

















The Dark Energy Survey supernova programme: modelling selection efficiency and observed core-collapse supernova contamination

M. Vincenzi ^{1,★} M. Sullivan ² O. Graur ^{1,3} D. Brout ^{4,†} T. M. Davis ⁵ C. Frohmaier ¹
 L. Galbany ⁶ C. P. Gutiérrez ² S. R. Hinton ⁵ R. Hounsell^{7,8,9} L. Kelsey ² R. Kessler^{10,11}
 E. Kovacs¹² S. Kuhlmann¹² J. Lasker ^{10,11} C. Lidman ^{13,14} A. Möller ¹⁵ R. C. Nichol¹ M. Sako⁹
 D. Scolnic ¹⁶ M. Smith ² E. Swann¹ P. Wiseman ² J. Asorey¹⁷ G. F. Lewis¹⁸ R. Sharp¹⁴
 B. E. Tucker¹⁴ M. Agüena^{19,20} S. Allam²¹ S. Avila²² E. Bertin^{23,24} D. Brooks²⁵ D. L. Burke^{26,27}
 A. Carnero Rosell^{28,29} M. Carrasco Kind^{30,31} J. Carretero³² F. J. Castander^{33,34} A. Choi³⁵
 M. Costanzi^{36,37} L. N. da Costa^{20,38} M. E. S. Pereira³⁹ J. De Vicente¹⁷ S. Desai⁴⁰ H. T. Diehl²¹
 P. Doel²⁵ S. Everett⁴¹ I. Ferrero⁴² P. Fosalba^{33,34} J. Frieman^{11,21} J. García-Bellido²² E. Gaztanaga^{33,34}
 D. W. Gerdes^{39,43} D. Gruen^{26,27,44} R. A. Gruendl^{30,31} G. Gutierrez²¹ D. L. Hollowood⁴¹
 K. Honscheid^{35,45} B. Hoyle^{46,47,48} D. J. James⁴⁹ K. Kuehn^{50,51} N. Kuropatkin²¹ M. A. G. Maia^{20,38}
 P. Martini^{35,52,53} F. Menanteau^{30,31} R. Miquel^{32,54} R. Morgan⁵⁵ A. Palmese^{11,21} F. Paz-Chinchón^{31,56}
 A. A. Plazas⁵⁷ A. K. Romer⁵⁸ E. Sanchez¹⁷ V. Scarpine²¹ S. Serrano^{33,34} I. Sevilla-Noarbe¹⁷
 M. Soares-Santos³⁹ E. Suchyta⁵⁹ G. Tarle³⁹ D. Thomas¹ C. To^{26,27,44} T. N. Varga^{47,48} A. R. Walker⁶⁰
 R. D. Wilkinson⁵⁸ and (DES Collaboration)

Affiliations are listed at the end of the paper

Accepted 2021 April 23. Received 2021 March 2; in original form 2020 December 10

ABSTRACT

The analysis of current and future cosmological surveys of Type Ia supernovae (SNe Ia) at high redshift depends on the accurate photometric classification of the SN events detected. Generating realistic simulations of photometric SN surveys constitutes an essential step for training and testing photometric classification algorithms, and for correcting biases introduced by selection effects and contamination arising from core-collapse SNe in the photometric SN Ia samples. We use published SN time-series spectrophotometric templates, rates, luminosity functions, and empirical relationships between SNe and their host galaxies to construct a framework for simulating photometric SN surveys. We present this framework in the context of the Dark Energy Survey (DES) 5-yr photometric SN sample, comparing our simulations of DES with the observed DES transient populations. We demonstrate excellent agreement in many distributions, including Hubble residuals, between our simulations and data. We estimate the core collapse fraction expected in the DES SN sample after selection requirements are applied and before photometric classification. After testing different modelling choices and astrophysical assumptions underlying our simulation, we find that the predicted contamination varies from 7.2 to 11.7 per cent, with an average of 8.8 per cent and an r.m.s. of 1.1 per cent. Our simulations are the first to reproduce the observed photometric SN and host galaxy properties in high-redshift surveys without fine-tuning the input parameters. The simulation methods presented here will be a critical component of the cosmology analysis of the DES photometric SN Ia sample: correcting for biases arising from contamination, and evaluating the associated systematic uncertainty.

Key words: surveys – supernovae: general – cosmology: observations.

1 INTRODUCTION

Type Ia supernovae (SNe Ia) are a mature and well-understood cosmological probe via their use as standardizable candles (Scolnic et al. 2019, and references therein). They remain a uniquely pow-

erful distance indicator in the high-redshift universe, and directly constrain the properties of dark energy. When combined with *Planck* cosmic microwave background (CMB) measurements, current SN Ia samples measure the dark energy equation-of-state parameter w with a precision of ~ 0.05 – 0.06 (Betoule et al. 2014; Scolnic et al. 2018; Dark Energy Survey 2019b), and show it to be consistent with a cosmological constant ($w = -1$).

With current and next-generation SN surveys [DES, Abbott et al. 2019; Legacy Survey of Space and Time (LSST), Ivezić et al.

* E-mail: maria.vincenzi@port.ac.uk

† NASA Einstein Fellow.

2019; Nancy Grace Roman Space Telescope, formerly *WFIRST*, Hounsell et al. 2018], statistical uncertainties on SN Ia cosmological measurements are becoming comparable to systematic uncertainties (Brout et al. 2019b). In this paper, we tackle some of the most important sources of systematic uncertainty related to SN Ia cosmological analysis and in particular we focus on core-collapse contamination and selection effects.

The Dark Energy Survey (DES) SN programme (DES SN) is the current state-of-the-art sample for SN Ia cosmology analysis. Over five seasons, this programme discovered and monitored more than 30 000 optical transients of various astrophysical origins. For 60 per cent of this sample, the spectroscopic redshift of the identified host galaxy has been measured (many via the OzDES programme; see Lidman et al. 2020) and approximately 570 transients have been spectroscopically confirmed and classified (e.g. Smith et al. 2020a).

The first cosmological results using SNe Ia from DES (DES-SN3YR) have been measured from a sample of 207 spectroscopically confirmed SNe Ia observed during the first three DES SN seasons, combined with 122 publicly available low-redshift SNe (Dark Energy Survey 2019a, b; Macaulay et al. 2019). Detailed descriptions of the analysis are presented by Brout et al. (2019a, b), Kessler et al. (2019b), Lasker et al. (2019), and Smith et al. (2020b). The final 5-yr DES SN sample will include not only spectroscopically confirmed SNe Ia, but also photometrically identified SNe Ia with a spectroscopic redshift measured from the identified host galaxy. This constitutes the DES photometric SN sample and it is an order of magnitude larger than the sample used for the first published cosmological results. This increases the statistical power of the DES SN sample significantly, but with the complication of additional sources of systematic uncertainties that need to be considered, e.g. those due to the photometric classification of the SNe, and due to the efficiency of measuring host galaxy redshifts.

The DES photometric SN sample includes a fraction of core-collapse SN events photometrically similar to SNe Ia but with a different astrophysical origin, and therefore different intrinsic brightnesses. Modelling this population of contaminants, and assessing the impact on cosmology, is one of the key challenges to fully exploit the DES photometric SN sample. This modelling is complex and depends on realistic simulations of core-collapse SNe, which can be combined with simulations of SNe Ia to build mock catalogues of the DES SN sample. These simulations are used for modelling selection effects and biases, and to generate training samples for SN classification algorithms, i.e. algorithms designed to identify the type of an SN from photometric data alone.

In the last decade, various SN photometric classifiers have been developed, and algorithms that exploit machine-learning techniques typically outperform other classifiers based on a template fitting approach (e.g. Lochner et al. 2016; Boone 2019; Möller & de Boissière 2020). However, the performance of machine-learning photometric classifiers is fundamentally dependent on homogeneous, representative and large training samples, with >100 000 events required in some cases. Unfortunately, spectroscopically confirmed SN samples are significantly more limited in size, usually biased towards brighter events and discovered in lower surface brightness local environments where it is easier to observe a spectrum with the signal-to-noise adequate for classification. Using such spectroscopically confirmed SN samples as training samples is therefore not a viable option, and instead representative training samples are typically generated with simulations.

For similar reasons, the validation and testing of photometric classifiers also require realistic simulations and cannot be performed on data alone. However, the training, validation, and testing of

photometric classifiers on samples (either real or simulated) can lead to overfitting and overestimations of sample purity, particularly if the training samples contain only a limited snapshot of the true astrophysical diversity of the SN population.

Therefore, tests of the true performances of photometric classifiers must be carefully designed to avoid overestimating the accuracy of these algorithms and, for future cosmological analysis, this is ultimately as important as developing photometric classification algorithms. The methods presented here aim to address this critical validation issue.

There have been many attempts to improve the simulations of core-collapse SNe. The initial set of core-collapse templates published for the Supernova Photometric Classification Challenge (SNPhotCC; Kessler et al. 2010a, b) has been updated with models of Type IIb SNe and SN1991bg-like SNe Ia from Jones et al. (2017) in order to augment the diversity of simulated contamination. The Photometric LSST Astronomical Time-Series Classification Challenge Team (PLAsTiCC; The PLAsTiCC Team et al. 2018; Kessler et al. 2019a; Hložek et al. 2020) further improved and expanded this library, including other types of transients and exploring other techniques to augment template diversity. Independently, a new library of core-collapse templates has been presented by Vincenzi et al. (2019). These templates are built from core-collapse SNe using high-quality photometry and spectroscopy, and they have been robustly extended to ultraviolet (UV) wavelengths. Simulations also rely on core-collapse SN luminosity functions and rates, for which several measurements have been recently published (Strolger et al. 2015; Graur et al. 2017; Shivvers et al. 2017; Vincenzi et al. 2019; Frohmaier et al. 2021).

There are many elements of uncertainty in simulations of core-collapse SNe, especially at intermediate and high redshifts. Most measurements of core-collapse SN demographics available in the literature are based on small and primarily low-redshift samples ($z \lesssim 0.05$), whereas SN surveys like DES probe a significantly larger range in redshift ($z \lesssim 1.2$). For example, results from the Pan-STARRS Medium Deep Survey (Jones et al. 2017, 2018) demonstrated that simulations based on currently published measurements of core-collapse SN global properties do not accurately reproduce the core-collapse contamination observed in high-redshift Hubble residuals. They find that in order to reproduce the contamination observed in the Pan-STARRS photometric SN sample, the luminosity functions from Li et al. (2011) need to be brightened by 1 mag, and the brightness dispersion for SNe Ib/c reduced by 55 per cent.

Finally, the effects of inaccurate modelling of core-collapse SNe are easily conflated with another important uncertainty in SN samples: selection effects. Simulations of photometric SN experiments like Pan-STARRS and DES require modelling of the SN detection efficiency and the efficiency of measuring host galaxy spectroscopic redshifts. While the SN detection efficiency has been robustly modelled for numerous surveys over the past decade using image-based simulations (e.g. Dilday et al. 2008; Perrett et al. 2012, and for DES, Kessler et al. 2015, 2019b), there is very limited work on how to model selection effects from host galaxy spectroscopic redshift surveys using a similar first principles modelling approach, and significant fine-tuning is usually applied.

In this paper, we present a set of realistic simulations of the DES photometric SN survey for which we significantly improve the modelling of core-collapse SNe and of the efficiency of measuring spectroscopic redshifts of SN host galaxies. The improvements in the core-collapse SN modelling are due to the implementation of high-quality templates and other published measurements of global core-collapse SN properties. To improve the modelling of

the spectroscopic redshift efficiency, we explore a novel, data-driven approach and model the spectroscopic redshift efficiency as a function of host galaxy properties. We improve the simulation of SN host galaxies, and associate hosts to simulated SNe using published measurements of SN rates as a function of galaxy properties. The simulations presented in this paper constitute the foundation for a robust estimation of cosmological biases due to the core-collapse SN contamination expected in the DES photometric SN sample.

We present an overview of the DES SN sample in Section 2, and describe how we estimate and model selection effects from the host spectroscopic redshift survey in Section 3. In Section 4, we present the baseline approach to build simulations of the DES photometric SN sample. In Section 5, we compare our simulations and the DES SN data set and we evaluate how well our simulations reproduce core-collapse SN contamination in the DES sample. In Section 6, we test how sensitive our results are to our assumptions and the choices of template libraries used to generate core-collapse SN simulations. We summarize in Section 7 and discuss future directions.

2 THE DES PHOTOMETRIC SN SAMPLE

DES is an optical imaging survey designed to constrain the properties of dark energy and other cosmological parameters by combining four different astrophysical probes: weak gravitational lensing, large-scale structure, galaxy clusters, and SNe Ia (Abbott et al. 2019). The imaging data are acquired by the Dark Energy Camera (DECam; Flaugher et al. 2015), mounted on the Blanco 4-m telescope at the Cerro Tololo Inter-American Observatory. DES surveyed 5000 deg² of the Southern hemisphere sky over 6 yr. For time-domain science, DES monitored 10 3-deg² fields with an average cadence of 7 d in the *griz* filters during the first 5 yr. Eight of these ten fields (X1, X2, E1, E2, C1, C2, S1, and S2) were observed to a single-visit depth of $m \sim 23.5$ mag (‘shallow fields’), and two (X3 and C3) to a depth of $m \sim 24.5$ mag (‘deep fields’).

In this section, we present the DES photometric SN sample. This is defined as the sample of SN Ia-like events discovered by DES over 5 yr of observations and for which a spectroscopic redshift for the identified host has been obtained. The discovery and photometry of DES SNe are presented in Section 2.1, and the host galaxy identification and spectroscopic redshift measurements in Sections 2.2 and 2.3, respectively. In Section 2.4, we discuss how SN Ia-like events are selected from the data, and their light curves fitted using SN Ia spectra energy distribution (SED) models. In this analysis, we neither discuss nor apply cuts based on SN Ia photometric classifiers, which are often used in SN cosmological analysis to improve the purity of photometrically selected SN samples. This is to intentionally enhance core-collapse contamination in the DES sample and better analyse the properties of this population of contaminants.

2.1 SN discovery and photometry

In DES SN, the Difference Imaging pipeline (DIFFIMG; Kessler et al. 2015) is used to discover and estimate the flux of new transients via image subtraction, comparing new observations with previously collected reference images. The detections are passed through an automated artefact rejection algorithm (AUTOSCAN; Goldstein et al. 2015).

DIFFIMG is an efficient tool for the rapid identification of transients and the estimation of their fluxes at the 2 per cent level. However, it does not provide photometric measurements at the level of precision and accuracy required for SN Ia cosmology. The DES SN 3-yr (DES-SN3YR) cosmological analysis therefore used the technique of scene modelling photometry (SMP; Holtzman et al. 2008; Astier

et al. 2013; Brout et al. 2019a). The SMP algorithm simultaneously models the time-varying flux of a transient and the time-independent background flux from the host galaxy. SMP does not require image remapping and it determines robust uncertainties. However, it is computationally more expensive to run compared to DIFFIMG. The ongoing effort of running SMP on the full DES SN sample will be important for cosmological measurements and it will help in reducing systematic effects related to uncertainties on SN flux estimates; however, the DIFFIMG photometry is adequate for developing the modelling methods and simulations that are presented in this paper.

We use as our initial sample of candidate SNe all DES events with at least two detections (in any filter, separated by at least one night) with a signal-to-noise ratio (SNR) greater than 5, and that passed AUTOSCAN. These criteria are designed to remove asteroids and artefacts, while allowing relatively low SNR detections to be included. The total number of photometric transients that pass these requirements is roughly 30 000. We emphasize that not all of these transients are SNe, and certainly not all the SNe have adequate light-curve quality and redshift information to be used for cosmological measurements.

During survey operations, the light curve of each DES transient was also fitted with the Photometric SuperNova Identifier software PSNID (Sako et al. 2011), an SN photometric classifier tool based on template fitting techniques. This code provided an estimate of the time of peak brightness and a preliminary classification of the SN type.

2.2 Spectroscopic follow-up

Spectroscopic redshift information on the DES SN candidates is available from a number of sources:

- (i) During the course of the DES survey, a wide range of telescopes was used for the spectroscopic follow-up of DES SN candidates (e.g. Smith et al. 2020a). These spectra provide SN classifications and redshifts based on SN spectral features.¹
- (ii) The same telescope programmes also provide spectroscopic redshift measurements from host galaxy spectral features appearing in the SN spectra.
- (iii) Using the AAOmega spectrograph on the 3.9-m Anglo-Australian Telescope (AAT), spectroscopic redshifts for thousands of galaxies identified as hosts of DES transients were measured as part of the OzDES programme (Yuan et al. 2015; Childress et al. 2017; Lidman et al. 2020). The OzDES survey is the primary source of spectroscopic redshifts in the DES photometric SN sample.
- (iv) Various external redshift catalogues are available in the literature from spectroscopic surveys in the same fields as those monitored by DES SN.

Each source of spectroscopic redshift introduces different selection effects in the DES SN sample. We describe how these selection effects are modelled in Section 3.

2.3 Host galaxy association

For each DES transient, the most likely host galaxy has been identified using the directional light radius (DLR) method (Sullivan et al.

¹The list of telescopes used for the spectroscopic follow-up of DES SN candidates includes the 4-m AAT, the European Southern Observatory Very Large Telescope, Gemini, Gran Telescopio Canarias, Keck, Magellan, MMT, and South African Large Telescope.

2006; Gupta et al. 2016) applied to galaxies in the SVA1-COADD GOLD image catalogue (Rykoff et al. 2016). This catalogue uses data in the DES SN fields collected during the DES ‘Science Verification’ (SV) survey. Within the OzDES survey, a galaxy identified as the host of a DES transient is spectroscopically observed if the following criteria are satisfied:

(i) The galaxy has the smallest DLR among all catalogue entries and has $DLR < 7$, is brighter than 24.5 mag in the r band, is not flagged as a star (see Wiseman et al. 2020, for more details), and is not in a catalogue of known variable stars and active galactic nucleus (AGN; the so-called ‘VETO’ catalogue);

(ii) At least 30 per cent of the detections of the transient passed AUTOSCAN; the transient has at least one detection with an $SNR > 5$ in two filters, and at least one filter with two detections with an $SNR > 5$;

(iii) The transient is not detected in multiple seasons (i.e. it is not a long-duration transient such as a superluminous SN, a likely AGN, or a variable star);

(iv) The day of peak brightness estimated by PSNID fitting lies within a DES season.

This set of criteria defines the list of OzDES targets. If a spectroscopic redshift has already been measured by a published redshift survey, or if a spectroscopic redshift has been measured from galaxy features in a live SN spectrum, the galaxy is assigned a lower priority or not targeted at all. In this analysis, we consider OzDES spectroscopic redshifts measured with a confidence level higher than 95 per cent² and, if multiple sources of spectroscopic redshift are available for the same host galaxy, we select the OzDES spectroscopic redshift as the more accurate redshift.

After using these host galaxy associations and measurements in the DES-SN3YR analysis, high-quality depth-optimized coadds have been published by Wiseman et al. (2020). These coadds have been built combining the highest quality DES SN images taken before and well after SN detection, with a limiting magnitude of $g \sim 27$ mag, around 1–1.5 mag deeper than the SV data. As discussed by Wiseman et al. (2020), the host galaxy association was revised when upgrading from SV data to the deeper coadds: $\simeq 1.1$ per cent of SNe matched to a potential host in SV data had a different host identified with the new coadds. We use these revised associations, and all host galaxy photometric properties are determined from the Wiseman et al. (2020) stacks. In this paper, we define the host galaxy apparent magnitudes, m^{host} , as the Kron-like `MAG_AUTO` magnitudes measured with `SEXTRACTOR` (Bertin & Arnouts 1996) from the deep coadds.

We identify 7697 galaxies that satisfy the OzDES selection cuts listed above. For 5049 galaxies, we have a secure redshift measurement, i.e. a redshift measurement with a confidence level higher than 95 per cent, either from OzDES or external catalogues. Table 1 contains a summary of the sources of redshifts.

2.4 SALT2 fitting and selection cuts

To standardize the SN Ia brightnesses, the light curves of DES transients with an identified host galaxy and spectroscopic redshift are fitted with the SALT2 light-curve model (Guy et al. 2007, 2010a). SALT2 fits provide an estimate of the epoch of SN peak brightness t_0 , a stretch-like parameter x_1 , a colour parameter c , and

²A spectroscopic redshift measured with a confidence level higher than 95 per cent corresponds to a quality flag $Q = 3$; see Lidman et al. (2020) section 4 for further details on the OzDES redshift flag scheme.

Table 1. Summary of redshift sources for DES SNe.

Redshift source	SN redshifts	Per cent of total
All	5049	–
OzDES	4419	87.52
Galaxy features in SN spectra	65	1.29
External catalogues	565	11.19
SDSS	136	2.69
VIPERS	105	2.08
2dF archival redshifts ^a	101	2.00
GAMA	99	1.96
NED	32	0.63
PanSTARRS+MMT	31	0.61
ACES	19	0.38
Others ^b	42	0.83
SN features in SN spectra ^c	81	–

^aArchival redshifts from DEVILS, LADUMA, and PanSTARRS SN survey.

^bOther external catalogues include VIMOS VLT Deep Survey (VVDS), ATLAS, MUSE, and Ultra Deep Survey (UDS).

^cSNe for which the *only* source of spectroscopic redshift is the SN spectrum itself, and either a faint host ($m^{\text{host}} > 24$ for 26 SNe) or no host (55 SNe, ‘hostless’ SNe) is detected in the deep coadds. These events are excluded from our analysis.

References: Tasca et al. (2017), Weiner et al. (2005), Newman et al. (2013), Scodreggio et al. (2018), Geha et al. (2017), Herenz et al. (2017), Colless et al. (2003), Baldry et al. (2018), Mao et al. (2010), Nanayakkara et al. (2016), Ahumada et al. (2020), Muzzin et al. (2012), Le Fèvre et al. (2013), Bradshaw et al. (2013), Davies et al. (2018), Jones et al. (2018), and Baker, Blyth & Holwerda (2019).

the normalization parameter x_0 . SALT2 model fitting is implemented with the `SNANA` light-curve fitting programme and uses the χ^2 minimization algorithm `MINUIT` to estimate the best-fitting value and uncertainty of each SALT2 parameter. The SALT2 parameters are then used to estimate the SN distance modulus, μ_{obs} , defined as (e.g. Tripp 1998; Astier et al. 2006)

$$\mu_{\text{obs}} = m_B + \alpha x_1 - \beta c + \mathcal{M}_B, \quad (1)$$

where m_B is defined as $-2.5 \log_{10}(x_0)$ and \mathcal{M}_B is the absolute brightness for an SN Ia with $x_1 = 0$ and $c = 0$. α and β are global nuisance parameters that ‘standardize’ the SN Ia brightnesses, usually determined from a global fit of the Hubble diagram. The residuals from a cosmological model $\Delta\mu$ (often termed ‘Hubble residuals’) are then defined as

$$\Delta\mu = \mu_{\text{obs}} - \mu_{\text{theory}}(C, z), \quad (2)$$

where μ_{theory} is the theoretical distance modulus, which is dependent on the cosmological parameters, C .

In our analysis, we assume $\mathcal{M}_B = -19.365$ and we set α and β equal to the values measured by Dark Energy Survey (2019b), i.e. $\alpha = 0.146$, $\beta = 3.03$. For both observed and simulated SNe, we measure SN distance moduli, μ_{obs} , fixing these nuisance parameters. The values of α and β found by Dark Energy Survey (2019b) are also used as the input values for the simulations. We calculate Hubble residuals assuming a flat Λ CDM cosmological model with Hubble constant $H_0 = 70 \text{ km s}^{-1} \text{ Mpc}^{-1}$ and $\Omega_M = 0.311$ (following Planck Collaboration VI 2020). While these Hubble residuals are very useful for evaluating our simulations, we note that they do not have the level of accuracy required for a cosmological measurement for several reasons: they are measured from `DIFFIMG` photometry, we have not included bias corrections for the SN population, we have not included

Table 2. DES photometric SN sample: a summary of data cuts.

Data cut	Number remaining	Number rejected
SNe associated with a spectroscopic redshift	5049 ^a	–
Fit by SALT2	3627 ^b	–
‘transient_status’ flag	3401	226
Visual inspection	2802	599 ^c
Loose SALT2-based cuts	2553	249
SALT2-based cuts from Betoule et al. (2014)	1683	947

^aIncluding 54 SNe/hosts located in the DECam inter-CCD chip gaps;

^bWe exclude events for which the redshift is estimated from SN spectral features in the SN spectrum;

^cOut of the 599 visually inspected events, only 112 would pass the loose SALT2 cuts and only 8 would pass the Betoule et al. (2014) SALT2-based cuts.

SN systematic uncertainties, and therefore we have not optimized the values of α and β .

To ensure meaningful light-curve fits with the SALT2 model the following selection requirements are applied: (i) two filters with at least one epoch with an SNR > 5 , (ii) at least one data point before the time of peak brightness t_0 , and (iii) at least one data point 10 d after t_0 . Out of 5049 transients with a host galaxy redshift, 3627 satisfy these criteria and are successfully fitted with the SALT2 model.

This sample of events includes a significant fraction of transients that are clearly not SNe Ia or core-collapse SNe (e.g. AGN, variable stars, or long-duration transient events). We use the ‘transient_status’ flag defined by Smith et al. (2020a) to identify multiseason transients, which removes 226 events. Finally, we visually inspect all the remaining transients, and remove artefacts and events that show long-term variability (removing an additional 599 events). These single-season requirements reduce the sample to 2802 visually confirmed SN-like events.

After light-curve fitting, we consider two sets of additional requirements based on the fitted SALT2 parameters:

(i) ‘Loose’ SALT2-based cuts ($x_1 \in [-4.9, 4.9]$ and $c \in [-0.49, 0.49]$). This set of cuts intentionally enhances contamination in the data, and therefore allows us to better analyse the properties of contamination in our sample. After applying these cuts, 249 additional SNe are rejected from the sample (i.e. 2553 SNe remain);

(ii) The set of SALT2 cuts applied by Betoule et al. (2014) and Jones et al. (2017) ($x_1 \in [-3, 3]$, $c \in [-0.3, 0.3]$, $\sigma_{x_1} < 1$, $\sigma_{\text{peakMJD}} < 2$ d, and fit probability > 0.01).³ These cuts are generally adopted in SN Ia cosmology analyses to control contamination from peculiar SNe Ia or other peculiar thermonuclear SNe that are not well described by a SALT2 model. This set of cuts reduces the data to 1606 SNe (approximately 30 per cent of the sample is rejected).

In Table 2, we report a summary of the various cuts.

3 SPECTROSCOPIC REDSHIFT EFFICIENCY

As part of an SN Ia cosmology analysis, modelling selection effects is essential to estimate bias corrections and simulate training samples. Detection efficiency and photometric instrumental effects for the DES SN programme have been characterized and presented by Kessler et al. (2015). In this analysis, we mainly focus on selection

³Fit probabilities are based on the fit reduced χ^2 and quantify how well each light curve is described by the SALT2 model assuming that the photometric uncertainties are Gaussian.

effects due to the requirement of a host galaxy spectroscopic redshift. This is a critical selection effect in the DES SN data set – it shapes the redshift distribution of the sample and introduces biases towards SNe in bright, emission-line galaxies for which measuring a spectroscopic redshift is easier.

In this section, we describe our approach for the modelling of the spectroscopic redshift efficiency ($\varepsilon_{z_{\text{spec}}}$), i.e. the overall efficiency of obtaining spectroscopic redshifts in DES and how we incorporate this in our simulations of the DES SN sample.

3.1 A novel approach to modelling selection effects

Previous analyses of photometric SN samples (Jones et al. 2017, 2019) have modelled $\varepsilon_{z_{\text{spec}}}$ as a one-dimensional function of redshift, tuning $\varepsilon_{z_{\text{spec}}}$ so that the simulations reproduce the observed redshift distribution. By construction, this efficiency function is tailored to a specific choice of volumetric SN rates, it does not depend on galaxy properties, and it is applied to all types of SNe. While this approach guarantees a good agreement in the redshift distribution between data and simulations, it does not account for brighter galaxies being more likely to get a spectroscopic redshift and, as a consequence, that SNe exploding in bright and high-mass galaxies are more likely to be selected.

Our approach is substantially different in two respects. First, we measure $\varepsilon_{z_{\text{spec}}}$ from the data – the sample of host galaxies that satisfy the criteria listed in Section 2.3, and therefore have been targeted in the OzDES survey. Secondly, we measure $\varepsilon_{z_{\text{spec}}}$ as a function of SN host galaxy properties. Using the sample of targeted galaxies, we calculate the fraction of galaxies with and without a spectroscopic redshift and measure the efficiency as a function of the host galaxy brightness and other observables, including the host galaxy $g - r$ colour and the epoch of SN discovery.

Our efficiency function can be integrated into simulations, but it in turn requires the simulations to include host galaxies with realistic properties. In particular, our simulations need to account for the strong dependence of SN rates on galaxy properties [for a given SN, not every galaxy is equally likely to be the host galaxy, depending on the galaxy stellar mass and/or the galaxy star formation rate (SFR)]. Using empirical SN rate models, the simulated host galaxies should reproduce the properties and brightness distributions of the observed SN host galaxies. This approach is fundamentally data driven, and takes into account the fact that different types of SNe explode in different populations of galaxies with different brightness distributions.

In this implementation, a good match between simulations and data is not guaranteed, as none of the parameters is tuned to ensure this. Our method also enables a novel independent astrophysical test of whether measurements of SN rates and their dependences on galaxy properties are well understood across the redshift range covered by the DES SN sample.

3.2 Efficiency of the spectroscopic redshift survey

Spectroscopic redshifts are available from various sources (Section 2.2), primarily from host galaxy spectral features and, when the live SN spectrum is available, from SN spectral features. When the redshift is measured from galaxy spectral features, $\varepsilon_{z_{\text{spec}}}$ depends primarily on the brightness of the host galaxy and the host spectral type. For a subset of 81 of the spectroscopically confirmed SNe (Table 1), the redshift can only be estimated from SN spectral features, and $\varepsilon_{z_{\text{spec}}}$ depends on the brightness of the SN on the epoch of spectroscopic observation. Therefore, including SN events for which

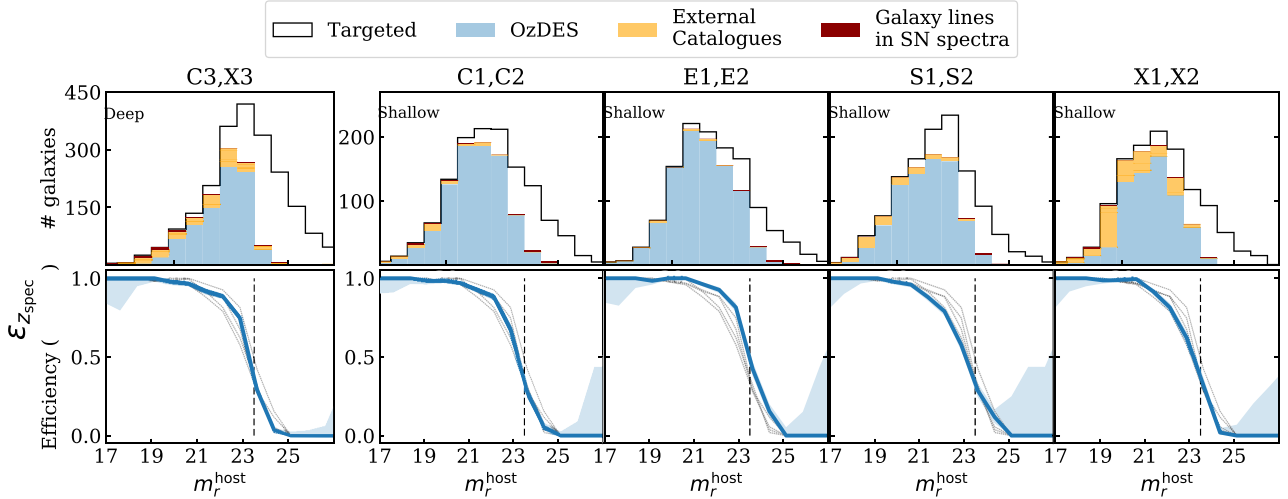


Figure 1. *Top panels:* For each pair of DES SN fields, we present distributions of m_r^{host} for all host galaxies that passed the OzDES selection criteria listed in Section 2.3 (black histogram), for host galaxies with a spectroscopic redshift from OzDES (light blue), from external catalogues (orange), and from galaxy emission lines in SN spectra (dark red). *Bottom panels:* We show $\epsilon_{z_{\text{spec}}}$ versus m_r^{host} for each pair of SN fields (blue thick line) and for all other SN fields (thin grey lines). The average host galaxy brightness is $m_r^{\text{host}} \simeq 23$ mag in the deep fields (X3 and C3) and $m_r^{\text{host}} \simeq 22$ mag in the shallow fields.

the *only* source of redshift is from the SN spectral features would require a very different and independent selection function (e.g. the selection functions presented in Kessler et al. 2019b; Smith et al. 2020a). This is beyond the scope of this analysis, and we therefore exclude this redshift information from this paper.

We measure $\epsilon_{z_{\text{spec}}}$ as a function of host galaxy brightness (Section 3.2.1), host galaxy observed colour (Section 3.2.2), and the year of discovery of the SN (Section 3.2.3). We define the efficiency as the ratio of the number of host galaxies for which a redshift is available (either from OzDES or other catalogues), over the total number of host galaxies that passed OzDES selection criteria. The OzDES selection criteria are listed in Section 2.3, which are different from the selection cuts used to define the final DES photometric SN sample (Section 2.4). We estimate uncertainties on $\epsilon_{z_{\text{spec}}}$ using the method described by Paterno (2004) and implemented in the SN detection efficiency calculations from Frohmaier et al. (2017).

3.2.1 Efficiency as a function of galaxy brightness

We first measure $\epsilon_{z_{\text{spec}}}$ as a function of m_r^{host} , presented in Fig. 1 for five sub-groups of DES SN fields. As expected, $\epsilon_{z_{\text{spec}}}$ is high for bright host galaxy magnitudes, in many cases 100 per cent, and drops sharply above $m_r^{\text{host}} \sim 21$ mag. The 50 per cent efficiencies range from $m_r^{\text{host}} \simeq 23$ to 23.5 mag.

The efficiency varies from field to field for several reasons. First, the two deep fields, X3 and C3, were prioritized by OzDES as they include more SN candidates due to the deeper DES data. Secondly, the E1 and E2 fields were observed more frequently as they have the longest visibility window from the AAT. Finally, some fields have more external redshifts available; for example, the X1 and X2 fields overlap with the GAMA survey (Baldry et al. 2018).

3.2.2 Efficiency as a function of galaxy spectral type

$\epsilon_{z_{\text{spec}}}$ depends not only on galaxy brightness but also on the galaxy spectral type (e.g. it is easier to measure redshifts for emission-line galaxies). This dependence affects the fraction of core-collapse SN contamination in our sample as these events almost exclusively

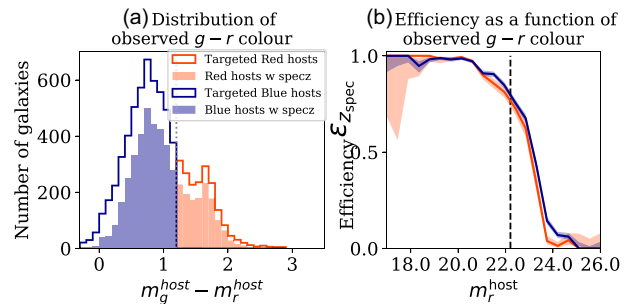


Figure 2. Panel (a): distribution of observed $g - r$ colours for all host galaxies that passed the OzDES targeting criteria (open histogram) and hosts with spectroscopic redshift (filled histograms). We define red galaxies as those with $g - r$ greater than 1.2, and blue galaxies as those with $g - r$ less than 1.2 (marked by the vertical dotted line). Panel (b): $\epsilon_{z_{\text{spec}}}$ versus m_r^{host} for both red and blue galaxies (red and blue solid lines). The median brightness of our sample of SN hosts is shown as the vertical dashed line, and it shows the magnitude at which most of the DES host galaxies are observed and therefore where discrepancies in efficiency have the largest impact.

explode in star-forming galaxies (Li et al. 2011). Since the spectral type is not available for all the targeted host galaxies, we consider alternative proxies of galaxy spectral type, such as the observed $g - r$ colour.

In Fig. 2, we present the distribution of observed $g - r$ colours for the sample of SN host galaxies that pass the OzDES criteria (see Section 2.3). We separately measure $\epsilon_{z_{\text{spec}}}$ for the 25 per cent ‘reddest’ galaxies in the sample and for the remaining sample of ‘bluer’ galaxies (this corresponds to a threshold of $g - r = 1.2$ mag). The efficiency measured from the sub-sample of ‘redder’ galaxies is systematically lower than that measured from ‘bluer’ galaxies (5 per cent lower at $m_r^{\text{host}} = 22$ mag and 15 per cent lower at $m_r^{\text{host}} = 23$ mag). We implement this colour dependence of $\epsilon_{z_{\text{spec}}}$ in our simulations. We note that this colour dependence is a second-order effect as the OzDES programme is optimized to achieve a high completeness to a magnitude limit of $m_r^{\text{host}} \sim 24$ and the OzDES strategy is to repeatedly target SN host galaxies until the level of confidence is larger than 99 per cent (see Lidman et al. 2020, for details).

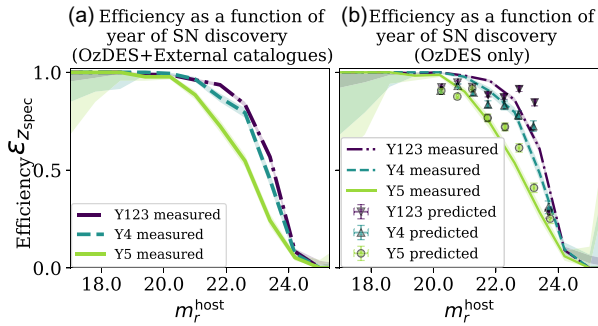


Figure 3. Panel (a): $\varepsilon_{z_{\text{spec}}}$ as a function of m_r^{host} for SNe discovered in the first, second, and third years of DES (2013–2015; dotted–dashed line), for SNe discovered in the fourth year of DES (2016; dashed line) and in the fifth year of DES (2017; solid line). The limited observing time towards the end of the OzDES programme caused a small drop in $\varepsilon_{z_{\text{spec}}}$ for Y4 and Y5. Panel (b): same as panel (a), but excluding galaxies with spectroscopic redshifts from external redshift catalogues. We compare $\varepsilon_{z_{\text{spec}}}$ measured from the ratio between galaxies with and without a spectroscopic redshift for the three different year bins [legend is same as panel (a)] with the $\varepsilon_{z_{\text{spec}}}$ inferred combining the information on OzDES exposure times with the OzDES completeness presented by Lidman et al. (2020) (see Section 3.2.3 for details).

3.2.3 Efficiency as a function of the year of SN discovery

The OzDES programme ran between 2013 (first year of the DES SN programme) and 2018 (1 yr after the end of the DES SN programme), so that host galaxies of SN discovered in the last year of DES could be observed. The number of nights allocated to OzDES was progressively increased each year (see Lidman et al. 2020, for details) in order to accommodate the increasing number of SNe discovered by DES. The amount of fibre hours available at the end of OzDES was not sufficient to achieve the same efficiency obtained for hosts of SNe discovered earlier in the DES survey. For this reason, we find that $\varepsilon_{z_{\text{spec}}}$ decreases for SNe discovered in the fourth and fifth years of DES.

We measure this trend by dividing the sample of host galaxies that passed OzDES selection criteria into three sub-groups, depending on the year of discovery of the hosted SN. We consider separately galaxies hosting SNe discovered in the first three years of DES, in the fourth year of DES, and in the fifth year of DES. We then measured the $\varepsilon_{z_{\text{spec}}}$ as a function of m_r^{host} in each sub-group. Our results are shown in Fig. 3(a).

The progressive decrease observed in $\varepsilon_{z_{\text{spec}}}$ can also be inferred knowing the observing time spent on each host galaxy and knowing the survey completeness as a function of exposure time. Exposure times are known for all galaxies targeted within the OzDES programme (but not for galaxies whose redshift is taken from external redshift catalogues) and the completeness of the OzDES programme is presented by Lidman et al. (2020) (see fig. 9). In Fig. 3(b), we compare the $\varepsilon_{z_{\text{spec}}}$ predicted using the information on exposure times and the $\varepsilon_{z_{\text{spec}}}$ directly measured from the fraction of galaxies with and without a spectroscopic redshift. The two methods give consistent results and this confirms that the trend observed is mainly caused by the progressively decreasing observing time available within the OzDES programme. In our simulations, we use the measured $\varepsilon_{z_{\text{spec}}}$ and we model this trend for each pair of SN fields shown in Fig. 1 separately.

4 SIMULATIONS

We next describe the simulations that underpin our study of the systematic uncertainties introduced by contamination from core-collapse SNe. These simulations are designed to produce a realistic

realization of the DES photometric SN sample. In the following section, we present the ‘Baseline’ simulation based on assumptions about the global properties of SNe Ia, peculiar SNe Ia, and core-collapse SNe. In Section 6, we present additional simulations and explore alternative core-collapse SN modelling assumptions.

4.1 Implementation in SNANA

Synthetic SN light curves are generated and analysed using the SuperNova ANALYSIS software (SNANA; Kessler et al. 2009),⁴ integrated in the PIPPIN pipeline framework (Hinton & Brout 2020).⁵ The SNANA simulation generates realistic transient light curves from one or more spectrophotometric models of transients. Kessler et al. (2019b, hereafter K19) present a detailed description of the simulations designed to characterize and reproduce SNe Ia within the DES SN survey, and in particular the DES-SN3YR sample. Here, we briefly describe the three main steps that constitute the SNANA simulation (see fig. 1 in K19 for a schematic illustration) and highlight the assumptions adopted in our analysis.

The first step is to generate a source SED model, selecting a specific SN population (see Sections 4.2, 4.3, and 4.4) and astrophysical effects that include host galaxy extinction, redshifting, cosmological dimming, lensing magnification, peculiar velocity, and Milky Way extinction. In our analysis, we use where necessary a Cardelli, Clayton & Mathis (1989) dust law with $R_V = 3.1$ for Milky Way and host galaxy dust extinction. The integration of the generated SED model over the DES filters provides an estimate of the ‘true’ magnitudes of the source before observational noise is applied.

The second step is to convert true magnitudes into observed fluxes and calculate the flux uncertainties. This step uses the observing conditions provided in a pre-computed observational library (referred to as a ‘simlib’). The simlib includes measured photometric zero-points, sky noise, and point spread function (PSF) information at 10 000 random sky locations within the DES fields. Flux uncertainties are estimated as the quadrature sum of the sky noise and the Poisson noise from the source and the surface brightness of the host galaxy. Host galaxies are selected from a galaxy catalogue (‘HOSTLIB’). In Section 4.5, we present the HOSTLIB used for our simulations and the recipe implemented for host galaxy association. Finally, the extra source of anomalous noise introduced by the DIFFIMG pipeline is estimated and robustly modelled using a set of separate image-based simulations for which ‘fake’ SNe are placed in real DES images and processed through the same DIFFIMG pipeline as applied to the data [see Kessler et al. (2015) and section 6.4 in K19 for an extended discussion].

The third and final step is to simulate the ‘trigger model’ for the selection of events. Detection efficiency versus SNR is implemented as described in section 7.1 in K19. Following the same DES trigger logic applied to real data, we select simulated events that have at least one detection on two separate nights.

In the following subsections, we describe the SED models used to simulate different astrophysics transients and their implementation in the simulation.

4.2 Simulations of ‘normal’ SNe Ia

We simulate normal SNe Ia, i.e. those that are used in cosmological fitting, using the SALT2 SED model presented by Guy et al. (2007) and trained on the Joint Lightcurve Analysis sample presented by

⁴<https://github.com/RickKessler/SNANA>

⁵<https://github.com/Samreay/Pippin>

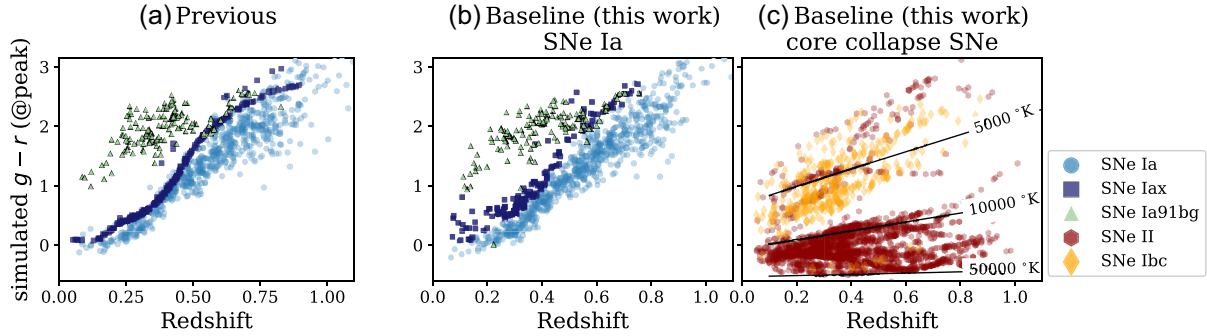


Figure 4. Simulated $g - r$ colours at peak brightness for various types of SNe as a function of redshift. In panel (a), SNe Ia are generated using the SALT2 SED model from Betoule et al. (2014), and SNe 91bg and SNe Iax using the original PLAsTiCC templates. In panel (b), SNe Ia are generated from the SALT2 SED model, and SNe 91bg and SNe Iax are simulated using the PLAsTiCC templates with the addition of dust extinction for SNe Iax and stretch diversity for SNe 91bg (see Section 4.3). In panel (c), core-collapse SNe are simulated using the V19 templates that include dust extinction as measured in the original events. This is the baseline simulation implemented in this analysis. For comparison with the $g - r$ colour evolution of core-collapse SNe, we also show the $g - r$ colour measured from blackbody SEDs at temperatures of 5000, 10 000, and 50 000 K.

Betoule et al. (2014). Each SN Ia is generated with random redshift, t_0 , x_1 , and c values. Redshifts are generated following the volumetric rate presented by Frohmaier et al. (2019), who combined published measurements from Dilday et al. (2008) and Perrett et al. (2012) with new measurements from the Palomar Transient Factory (PTF; Law et al. 2009). The t_0 values are randomly distributed within a time window that starts 2 months before the beginning of DES and finishes 2 months after the last visit of DES to the SN fields. The underlying distributions of x_1 and c are taken from Scolnic & Kessler (2016). For SN Ia intrinsic scatter, we adopt the ‘G10’ spectral variation model from Kessler et al. (2013) that is based on the wavelength-dependent scatter presented by Guy et al. (2010). Future analyses will explore in greater depth other approaches to simulating SNe Ia in DES, including different intrinsic scatter models (Brout & Scolnic 2020) and various effects of correlations between SNe Ia and host galaxy properties (Sullivan et al. 2006; Smith et al. 2012, 2020b; Rigault et al. 2018). In this analysis, the only SN Ia–host correlation that we model is between x_1 and host galaxy stellar mass (see Section 4.5 for details).

4.3 Simulations of peculiar SNe Ia

We include in our simulations two types of peculiar SNe Ia that may appear as photometric contaminants in SN Ia samples: SN1991bg-like SNe (Filippenko et al. 1992) and SN2002cx-like supernovae (Li et al. 2003; Foley et al. 2013, hereafter SNe Iax). SN1991bg-like (‘91bg-like’) SNe are sub-luminous compared to normal SNe Ia, and characterized by fast-declining (small x_1) light curves and redder colours at peak. In our simulations, we use the SED library of 35 91bg-like events presented in PLAsTiCC (Kessler et al. 2019a). In the original PLAsTiCC simulation, only five different SEDs were used and no stretch diversity was simulated (see section 4.2.2 in Kessler et al. 2019a) due to an error in the generation of the models. For our simulations, the PLAsTiCC team have provided us with the correct set of SED models. In Fig. 4, we present the $g - r$ colour synthesized at peak before observational noise is applied for our simulated 91bg-like SNe. This sub-class of peculiar SNe Ia is significantly redder at peak compared to normal SNe Ia.

SNe Iax (see Jha 2017, for a recent overview) generally rise and decline faster than normal SNe Ia and are characterized by low-velocity ejecta. Again, we use the model presented in PLAsTiCC, based on SN2005hk (Phillips et al. 2007; Sahu et al. 2008). As with normal SNe Ia, the absolute brightness of SNe Iax has been

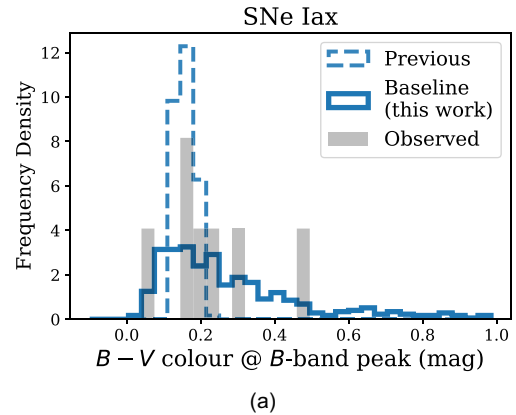


Figure 5. $B - V$ colour distribution at B -band peak for SNe Iax simulated using the original PLAsTiCC models (dashed histogram), for the updated SNe Iax model used in this analysis (solid histogram; Section 4.3), and for seven observed SNe Iax for which good B - and V -band photometry around peak has been published (grey-filled histogram, SN 2003gq, SN 2005cc, SN 2005hk, SN 2008A, SN 2008ha, SN 2011ay, and SN 2012Z from Silverman et al. 2012; Foley et al. 2013; Stahl et al. 2019).

shown to be correlated with light-curve width (Foley et al. 2013). To reproduce this correlation and expand the diversity of SN Iax models, the PLAsTiCC team generated multiple SN Iax SEDs by warping and renormalizing the original SN2005hk template. This reproduces the diversity of SNe Iax in terms of light-curve shape and normalization, but leaves the colour properties at peak unchanged (see Figs 4 and 5). The colour evolution and scatter of SNe Iax are poorly understood. However, as SNe Iax are believed to explode in younger environments (Takaro et al. 2020), and are therefore likely to be affected by dust, we opt to use dust extinction to introduce variation in the colour of the models. The reddening within the host galaxy for SN2005hk is estimated to be $E(B - V) = 0.09$ (Chornock et al. 2006), so we correct the PLAsTiCC SN Iax models for $E(B - V) = 0.09$, and apply a range of host extinctions in the simulations. We adopt the host extinction distribution described by Rodney et al. (2014) (which we also adopt for core-collapse SNe in the following sections), which allows us to well reproduce the colour diversity observed for SNe Iax (see Fig. 5).

Our revision of the original PLAsTiCC SN Iax models addresses the issues identified by Popovic, Scolnic & Kessler (2020). They

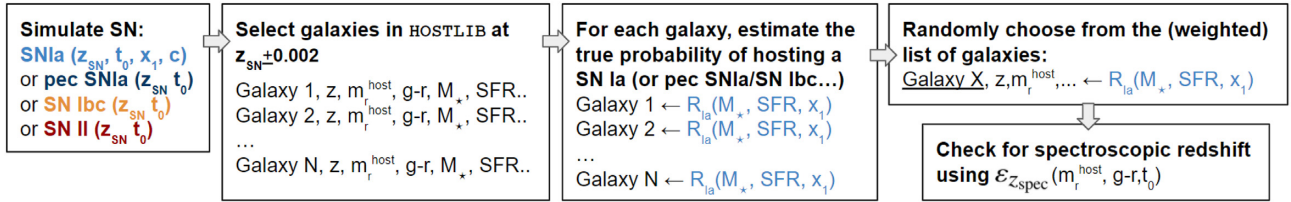


Figure 6. Flow chart describing the host galaxy association in the SNANA simulations. Here, we show an example of host galaxy association for SNe Ia, but the same general process applies to other SN types. Equations (3), (4), and (6) in Sections 4.5.1 and 4.5.2 describe SN rates as a function of galaxy properties (and additionally x_1 for SNe Ia) for all the SN types included in our simulations.

included the PLAsTiCC SN Iax models in their simulations of the Sloan Digital Sky Survey (SDSS) photometric SN sample, and observed that this significantly overestimates the predicted contamination, with the simulated SNe Iax appearing bluer than other samples of observed SNe Iax (see Fig. 5).

4.4 Simulations of core-collapse SNe: baseline approach

Our Baseline core-collapse SN simulations use the library of 67 SED time-series templates presented by Vincenzi et al. (2019, hereafter V19). This library combines spectroscopy and multiband photometry from 67 well-observed core-collapse SNe across 6 different subclasses (SN II, SN IIb, SN IIc, SN Ib, SN Ic, and SN Ic-BL). Each template covers 1600–11 000 Å; the UV coverage, in particular, is critical when simulating core-collapse SNe at high redshift. Fig. 4 shows the redshift evolution of the simulated $g - r$ colour at peak for different types of core-collapse SNe compared to SNe Ia. We find that core-collapse events in our simulations have the expected colour evolution. Stripped-envelope SNe are systematically redder at peak compared to SNe Ia. SNe II, however, are significantly bluer events and they follow the colour evolution expected from blackbody SEDs at different temperatures.

By construction, the V19 template library is biased towards bright core-collapse SNe and may not be representative of the intrinsic brightnesses and relative rates of different sub-types. Luminosity distributions and relative rates are generally measured from magnitude-limited samples such as the Lick Observatory Supernova Survey (LOSS) sample (Leaman et al. 2011; Li et al. 2011). As the SN events in the LOSS sample do not have sufficient data quality to construct SED templates, we adopt a hybrid approach and use the biased sample of SN events in the V19 template library and normalize it to brightnesses and rates measured from the LOSS sample.

For core-collapse SN relative rates, we use the measurements presented by Shivvers et al. (2017). Using the LOSS sample and revising the Li et al. (2011) measurement, Shivvers et al. (2017) showed that in the local universe SNe II and stripped-envelope SNe represent 69.6 per cent and 30.4 per cent of all core-collapse SNe, respectively. Frohmaier et al. (2021) find a similar result using data from PTF. Given the lack of measurements of relative rates at higher redshifts, in our Baseline simulation we assume that these relative rates do not evolve with redshift. We simulate core-collapse SNe assuming that the rate follows the cosmic star formation history presented in Madau & Dickinson (2014) normalized by the local SN rate of Frohmaier et al. (2021).

For the luminosity functions, the baseline simulation uses the mean and r.m.s absolute brightnesses measured from the LOSS sample, and we interpret these measurements as Gaussian luminosity functions. These were revised in V19 following updated classifications published by Shivvers et al. (2017) and they are reported in Table 5. We use the set of V19 templates that has not been corrected for host-

galaxy dust extinction because the revised Li et al. (2011, hereafter L11) luminosity functions are also measured from SNe not corrected for host-galaxy dust extinction. As described by V19, each sub-type of template is matched to its respective luminosity function applying *sub-type-dependent* magnitude offsets and dispersion.

The simulated core-collapse SN contamination can vary significantly depending on the choice of luminosity function, on whether additional host extinction is simulated, and on the adopted distribution of host-galaxy dust extinction. As most of these quantities are poorly constrained (especially at high redshift), we do not rely on one single core-collapse SN simulation but instead design a set of simulations that explore these different assumptions, and we test how our modelling choices affect our analysis. In Section 6, we present in detail each core-collapse simulation built for this analysis.

4.5 Simulating host galaxies

The rates of SNe in galaxies depend on the galaxy properties, such as stellar mass (M_*), SFR, and metallicity (Sullivan et al. 2006; Lampeitl et al. 2010; L11; Smith et al. 2012; Johansson et al. 2013; Graur, Bianco & Modjaz 2015; Graur et al. 2017; Rigault et al. 2018). For any given SN type, not every galaxy is equally likely to be a host and, in addition, the likelihood of an SN host having a spectroscopic redshift depends on the galaxy properties (see Section 3.2). Therefore, realistic simulations require an accurate modelling of how the SN rate and $\varepsilon_{z_{\text{spec}}}$ are correlated with galaxy properties. In this section, we discuss our approach in the simulations. A schematic illustration of galaxy association is presented in Fig. 6.

4.5.1 Simulating host galaxies of SNe Ia

We model correlations between SN Ia rates and galaxy properties following a two-component parametrization (the ‘A + B’ model) introduced by Mannucci et al. (2005). In this approach, the SN Ia rate is described as the sum of two terms:

$$R_{\text{Ia}}^{A+B}(M_*, \text{SFR}) = A \times M_* + B \times \text{SFR}. \quad (3)$$

This model was implemented by Sullivan et al. (2006) to analyse the Supernova Legacy Survey (SNLS) SN Ia sample. We use the best-fitting A and B parameters presented by Sullivan et al. (2006).

To model the well-known correlation between SN Ia x_1 and host galaxy M_* (e.g. fig. 4 in Smith et al. 2020b), we multiply the SNLS SN Ia rate in equation (3) by an additional term $[R_{\text{Ia}}^*(x_1, M_*)]$ so that the rate of SNe Ia in galaxies with $M_* < 10^{10} M_{\odot}$ drops monotonically to zero with decreasing x_1 . After analysing the DES-SN3YR SN Ia sample and comparing the tail of SNe Ia with $x_1 < 0$ in high-mass galaxies ($M_* > 10^{10} M_{\odot}$) and low-mass galaxies ($M_* < 10^{10} M_{\odot}$), we model the relative probability of having an SN Ia with a SALT2

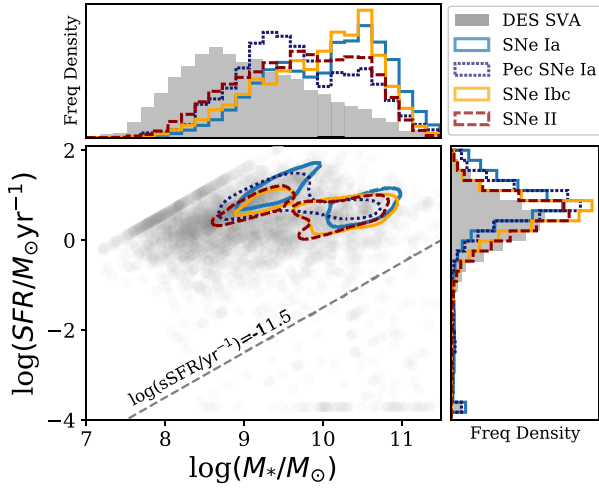


Figure 7. Distribution of galaxy SFR [$\log(\text{SFR})$] versus galaxy stellar mass [$\log(M_*)$] for all galaxies in the HOSTLIB (grey symbols and filled grey histograms) and for four different types of simulated SNe: SNe Ia (solid blue line), peculiar SNe Ia (91bg-like and SNe Iax; dotted blue line), SNe Ibc (solid orange line), and SNe II (dashed red line). The central 2D plot shows the 68 per cent density contour for each SN type. Different types of SNe are associated with host galaxies following the SN rates presented in Section 4.5. The dashed grey line separates our definition of star forming [above the line, i.e. $\log(\text{sSFR}) > -11.5$] and passive galaxies [below the line, i.e. $\log(\text{sSFR}) < -11.5$].

stretch x_1 in a galaxy with stellar mass M_* as

$$\begin{aligned} R_{\text{Ia}}^*(x_1, M_*) &= e^{-x_1^2} && \text{for } x_1 < 0 \text{ and } M_* < 10^{10} M_\odot \\ R_{\text{Ia}}^*(x_1, M_*) &= 1 && \text{for } x_1 > 0 \text{ and } M_* < 10^{10} M_\odot \\ R_{\text{Ia}}^*(x_1, M_*) &= 1 && \text{for } \forall x_1 \text{ and } M_* > 10^{10} M_\odot. \end{aligned} \quad (4)$$

As a result, the net rate applied for SNe Ia is

$$R_{\text{Ia}}(M_*, \text{SFR}, x_1) \propto R_{\text{Ia}}^{A+B}(M_*, \text{SFR}) \times R_{\text{Ia}}^*(x_1, M_*). \quad (5)$$

A more rigorous approach would be to implement a rate model that simultaneously fits the dependences on galaxy stellar mass, galaxy SFR, and SN Ia x_1 . Given that such a rate model has not been published yet, we decide to improve this aspect of our analysis in future work, also taking advantage of several recently published and ongoing analyses on the modelling of SN–host correlations and SN Ia rates (Popovic et al. 2021, Wiseman et al. 2021). For peculiar SNe Ia, we apply the same SN rate model used for normal SNe Ia with some variations. 91bg-like SNe Ia primarily explode in E/S0 galaxies (Howell 2001; L11), while SNe Iax are rarely found in early-type galaxies (Takaro et al. 2020). Therefore, we set the rate of 91bg-like (SNe Iax) to be zero in star-forming (passive) galaxies. In our analysis, a galaxy is defined as passive if its specific star formation rate (sSFR; the star-formation rate per unit stellar mass) is smaller than $10^{-11.5} \text{ yr}^{-1}$ (Fig. 7).

4.5.2 Simulating host galaxies of core-collapse SNe

Core-collapse SNe occur almost exclusively in star-forming galaxies (L11; Kelly & Kirshner 2012; Graur et al. 2017). Graur et al. (2017) measured the core-collapse SN rate as a function of galaxy properties for stripped-envelope SNe and SNe II, respectively. These rates are calculated using core-collapse SNe in the LOSS sample and are presented as a function of M_* , which is correlated with SFR for star-forming galaxies. Following these measurements, we model core-

collapse SN rates as

$$\begin{aligned} R_{\text{Ibc/II}} &= 0 \text{ in passive galaxies} \\ R_{\text{Ibc}}(M_*) &\propto (M_*/M_\odot)^{0.36} \\ R_{\text{II}}(M_*) &\propto (M_*/M_\odot)^{0.16}. \end{aligned} \quad (6)$$

Graur et al. (2017) show that SNe II have a shallower dependence on M_* compared to stripped-envelope SNe, and this result has a statistical significance of $>2\sigma$. This difference implies that the ratio between stripped-envelope SNe and SNe II (that on average is roughly 0.435; see Shivvers et al. 2017) varies depending on the host galaxy M_* ; stripped-envelope SNe are 10 times less common than SNe II in low-mass galaxies, but almost one-third of the SN II rate in high-mass galaxies. At higher redshifts, the DES photometric SN sample is biased towards brighter and more massive galaxies as they are more likely to get a spectroscopic redshift. This bias affects the composition of core-collapse SN contamination as a function of redshift and is modelled in our simulations.

4.5.3 Host galaxy association in simulations

Following Smith et al. (2020b), we select SN host galaxies from a HOSTLIB (Section 4.1) generated from the DES SV data. This catalogue includes $\sim 380\,000$ galaxies for which quantities like redshift (spectroscopic or photometric), galactic coordinates, magnitudes, and Sérsic profiles (Sérsic 1963) have been measured. For each HOSTLIB galaxy, M_* and SFR are measured using the method presented by Smith et al. (2020b) (see section 2.2.2).

The completeness of the DES SV HOSTLIB is >99 per cent for $m_i^{\text{host}} < 23.8$ mag and 50 per cent for $m_i^{\text{host}} < 24.75$ mag. Analysing the SNLS spectroscopic SN Ia sample (Sullivan et al. 2010), the fraction of SNe Ia in galaxies fainter than 23.8 is less than 15 per cent for $z < 0.8$ and approximately 30 per cent at $z = 1$. This fraction is likely to be higher for core-collapse SNe that on average explode in fainter galaxies. The depth of the DES SV HOSTLIB is one of the limiting factors in our analysis and may result in an overestimate of SNe at higher redshifts. We will explore the implementation of deeper HOSTLIB catalogues in future articles.

In our simulations, the SN-to-galaxy association is implemented as follows (see Fig. 6 for a schematic illustration). For an SN event simulated at redshift z , we select all HOSTLIB galaxies within the interval $z \pm 0.002$. Each galaxy within this redshift interval is then weighted by the SN rate (Sections 4.5.1 and 4.5.2), so that high-mass galaxies are favoured and the large fraction of faint, low-mass galaxies are given lower weight. The host is then randomly selected from the weighted list of galaxies. We identify the location of the SN within a host assuming that the distribution of SNe within their host galaxies follows the galaxy light profile (Kelly, Kirshner & Pahre 2008). For each epoch, the simulation computes the host galaxy flux within the $2\sigma_{\text{PSF}}$ radius aperture from the location of the SN and this Poisson variance is added to the flux variance. This galaxy variance affects the signal-to-noise of the SN flux and its likelihood of being detected. Finally, given the m_r^{host} and $g - r$ colour of the selected host galaxy, as well as the year of discovery of the simulated SN, we apply the efficiency $\varepsilon_{z,\text{spec}}$ (Section 3) to determine whether a redshift is measured.

Our method for the simulation of SN host galaxies is a significant improvement over earlier work. Our approach accounts for the fact that SNe of different astrophysical origins occur in different types of galaxies with different rates. Using our baseline simulation, we show in Fig. 7 how simulated host galaxies of different types of SNe have different distributions in terms of simulated M_* and SFR. Compared

to published samples of SNe Ia and core-collapse SNe (L11; Perley et al. 2020; Wiseman et al. 2020), our simulations reproduce the observed host galaxy properties: The population of SN Ia hosts is significantly skewed towards high-mass galaxies, with a significant fraction of events found in passive environments, while core-collapse SNe are preferentially hosted in star-forming galaxies with a larger fraction of events found in lower mass galaxies.

5 COMPARISON BETWEEN SIMULATIONS AND THE DES PHOTOMETRIC SAMPLE

In Section 4, we presented the Baseline framework of our simulation, the goal of which is to produce a simulation that matches the observed SN populations and properties of the DES photometric SN sample. In this section, we compare our Baseline simulation with the DES photometric SN sample presented in Section 2.4. This comparison constitutes the core of this paper, and is essential to test the astrophysical assumptions used in our simulations.

We present the simulation versus data comparisons for distributions of SN redshift, SALT2-fitted SN parameters, and Hubble residuals as described in Section 2.4. To first order, the Hubble residual distribution of SNe Ia can be modelled as a symmetric Gaussian, with a mean of zero and a standard deviation equal to the combination of intrinsic scatter of the SN Ia sample and observational noise. Due to the presence of core-collapse SN contamination, however, the Hubble residual distribution of a sample of photometrically classified SNe Ia will typically have an asymmetrical positive tail (Campbell et al. 2013; Jones et al. 2017).⁶ core-collapse SNe have, on average, fainter intrinsic brightnesses than SNe Ia, and are not standardizable using equation (1). Applying the same equation to an intrinsically fainter SN (like a core-collapse SN) leads to an overestimate of the SN distance modulus and thus positive Hubble residual (equation 2).

In Figs 8 and 9, we present a comparison between our Baseline simulation and the DES photometric SN sample for the distributions of SALT2 parameters (m_B , x_1 , c , and t_0) and their uncertainties, redshift, maximum observed SNR, and Hubble residuals. In Fig. 10, the same comparison is presented for m_r^{host} and host galaxy observed $g - r$ colour. We present results for deep and shallow fields separately, using the set of loose SALT2 cuts described in Section 2.4. We combine 25 realizations of the Baseline simulation (total of 60 000 simulated SNe) and normalize each histogram so that the total number of SNe in the simulation is equal to the total number of observed SNe (for deep and shallow fields separately). We evaluate the level of agreement between data and simulation by calculating the reduced chi-square χ_v^2 (the χ^2 per degree of freedom) as described by Brout et al. (2019b, section 3.7.3). We report the χ_v^2 in each figure panel.

Qualitatively, the simulation reproduces the DES SN sample well. This is a remarkable result considering the various assumptions that underpin the simulation (e.g. the SN rates, host galaxy properties, and SN templates), and considering that the inputs to the simulation have not been tuned to match the data. In detail, in Figs 8 and 9, we observe the following:

(i) In the x_1 distribution, both data and simulation contain a tail of high- x_1 events. This is caused by highly energetic stripped-envelope SNe (SNe Ic, SNe Ic-BL), often characterized by slowly evolving

light curves, and by faster declining SNe II compared to the general SN II population, but which are still slower than SNe Ia.

(ii) In the c distribution, data and simulations show tails at bluer and redder colours. The bluer tail is caused by SNe II, similar to hot blackbodies at peak and thus with bluer colours than SNe Ia. The redder tail is mainly due to SNe Iax and stripped-envelope SNe (see Figs 4 and 12 for a visualization of where stripped-envelope SNe and SNe II lie in colour space compared to SNe Ia).

(iii) The distribution of simulated t_{peak} matches the data well, suggesting that the time dependence of the spectroscopic redshift efficiency presented in Section 3.2.3 is well modelled.

(iv) The faint tail in the Hubble residuals, the clearest feature of the presence of contamination in the data, is also well reproduced. The ratio between the number of SNe with large Hubble residuals (>0.5 , i.e. likely contaminants) and the number of SNe with small Hubble residuals (<0.5 , i.e. likely SNe Ia) is 0.20 in data and 0.21 in simulations for the shallow fields. For deep fields, these numbers are 0.34 and 0.30, respectively. In photometric SN sample analyses, this is the first time that the contamination observed in the Hubble diagram is explained and almost fully reproduced by a simulation, without the requirement of significant fine-tuning of our assumptions and therefore lifting doubts on whether our knowledge of bright core-collapse SNe at high redshift presents substantial gaps. The only minor discrepancy we observe is that our simulation underestimates the contamination in the deep fields by about 10 per cent. The χ_v^2 is larger than that expected from statistical fluctuations, with probability-to-exceed values lower than 10^{-8} and 0.02 for the shallow and deep fields, respectively. The excess is mainly driven by the bulk population of SNe Ia at small Hubble residuals. These discrepancies arise because the Hubble residuals are measured assuming values of the nuisance parameters α , β , and \mathcal{M}_B , and assuming a cosmological model.

The fact that our simulation reproduces the main features that can be considered signatures of core-collapse contamination is promising. None the less, some discrepancies between simulations and observations should be noted.

(i) In the redshift distributions in Fig. 8, we note an underestimate of SN events at high redshift in the shallow fields, and in the deep fields we highlight that the sharp dip observed at a redshift (z) of ~ 0.5 is not correctly modelled by simulations;

(ii) The observed and simulated x_1 distributions agree well in the shallow fields but not in the deep fields. Shallow and deep fields probe slightly different redshift ranges and therefore different galaxy populations. SALT2 x_1 is known to be correlated with galaxy properties such as galaxy stellar mass, and this discrepancy suggests that our modelling of host mass- x_1 correlations and/or the HOSTLIB implemented needs to be improved;

(iii) The distribution of maximum SNR shows some discrepancies at lower values, which calls for further improvements in the modelling of flux uncertainties.

These discrepancies are unlikely to be solely due to an incorrect modelling of core-collapse SNe, as they occur in regions of the parameter space that are primarily dominated by SNe Ia (e.g. high redshift in the shallow fields, or near-zero Hubble residual in the deep fields). Further improvements in the modelling of flux uncertainties and selection effects in the DES data may be required, as well as the implementation of a deeper and more complete HOSTLIB that at high redshift will affect the fraction of SNe simulated in faint hosts, i.e. that are unlikely to have a spectroscopic redshift. Further revision of the modelling of SN Ia intrinsic properties (the intrinsic distributions

⁶Lensing magnification can also introduce an asymmetrical *negative* tail in the Hubble residual distribution. However, this effect is significantly smaller than the one introduced by core-collapse contamination and it is not discussed in this analysis.

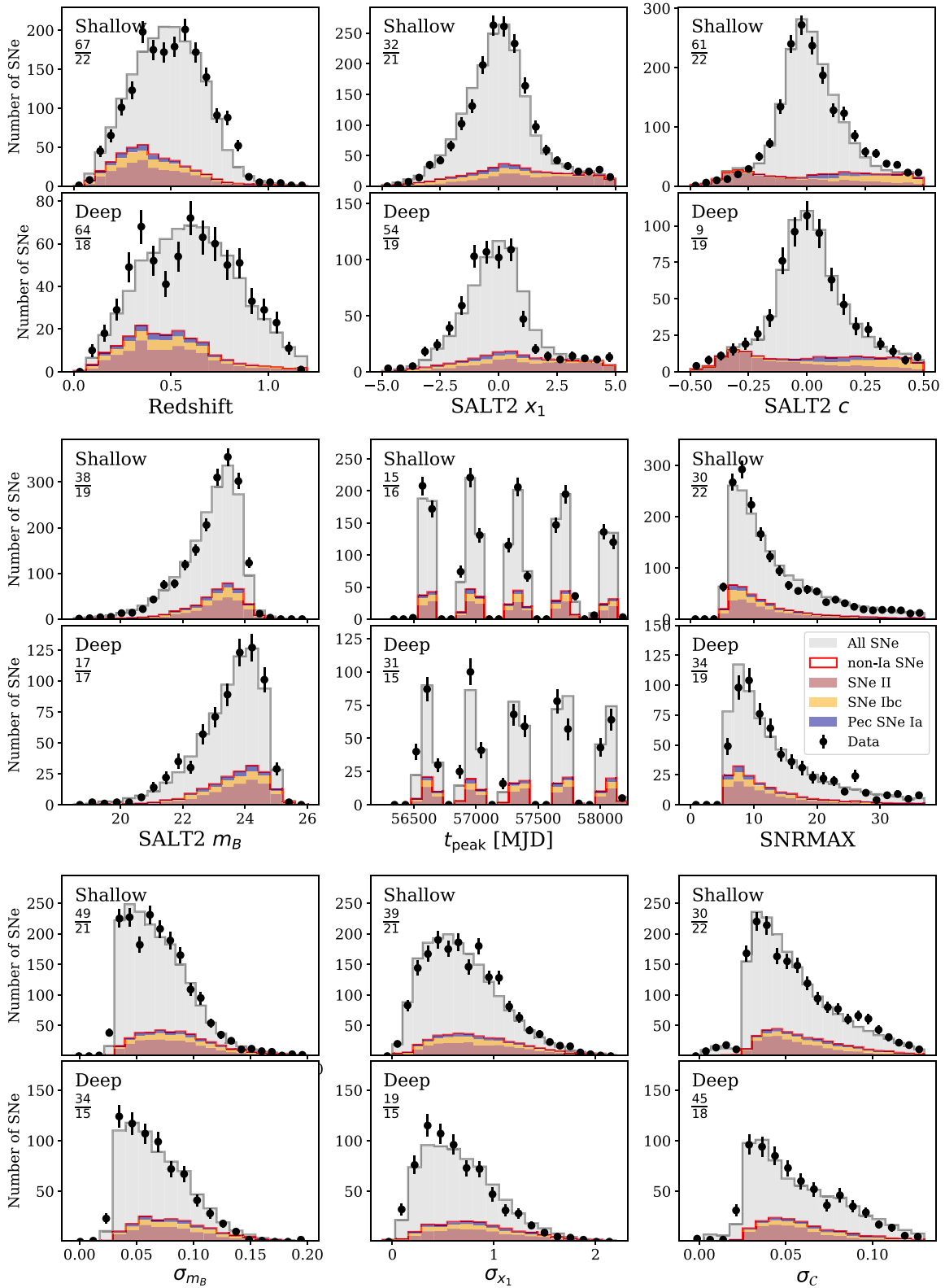


Figure 8. Various comparisons of our ‘Baseline’ simulations and data. The simulations include $\sim 60\,000$ SNe (25 realizations of the DES photometric SN sample) and the histograms are scaled to match the total number of events in the DES photometric sample. Top panels (from left to right): redshift, SN x_1 and SN c ; central panels: SN m_B , MJD of peak brightness, and maximum observed SNR; lower panels (from left to right): uncertainties in the SALT2-fitted parameters m_B , x_1 , and c . We compare data (black points), all simulated SNe (SNe Ia, peculiar SNe Ia, and core-collapse SNe combined; grey filled histogram), all non-Ia SNe (solid red line), SNe II (dark red filled histogram), SNe Ibc (stacked orange filled histogram), and peculiar SNe Ia only (stacked blue filled histogram). Results are presented for the shallow and deep fields separately. The χ^2_{ν} is reported in each panel.

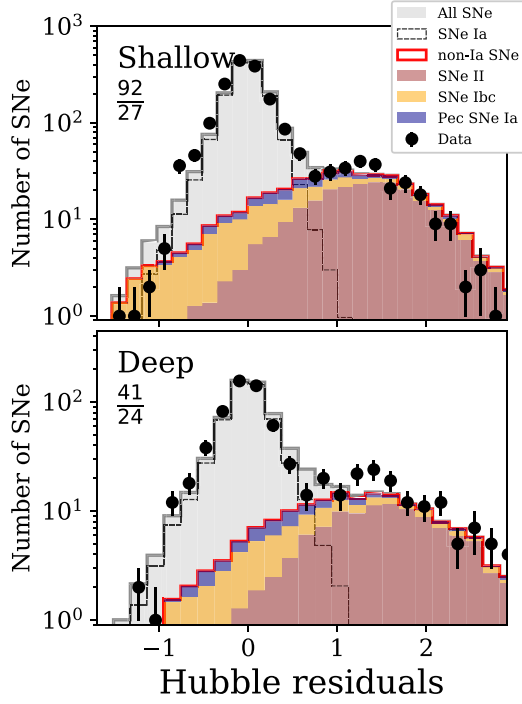


Figure 9. As Fig. 8 but for Hubble residuals.

of x_1 and c and the intrinsic scatter) may also be needed. These are all complex aspects of the analysis and we anticipate continued improvements in future analyses.

Finally, Fig. 10(b) shows that the observed distribution of m_r^{host} is well reproduced by simulations. This agreement suggests that the measurement of spectroscopic efficiency presented in Section 3 is robust, and that the implemented SN rate models (Section 4.5) adequately describe the data.

The importance of implementing a galaxy-dependent selection in our simulations is demonstrated in Fig. 10(a), the distribution of m_r^{host} from a simulation using the same inputs as the Baseline simulation, but with the exception that host galaxies are assigned randomly (i.e.

Table 3. True fraction of core-collapse SNe for different SALT2-based cuts.

Cut	Fraction of non-Ia SNe (per cent)	
	Only this cut	Exclude cut
Loose SALT2 cuts	22.5	–
$ x_1 < 3$	18.7	9.7
$ c < 0.3$	13.2	12.9
$\sigma_{x_1} < 1$ and $\sigma_{r_{\text{peak}}} < 2$	10.9	10.8
Fit prob > 0.001	8.2	10.9
Fit prob > 0.01	6.6	10.9

every galaxy has an equal probability of hosting an SN). Since the HOSTLIB implemented in our simulations is complete to $m_r \simeq 23.8$ mag, at redshifts lower than 0.4–0.5 it is dominated by faint and low-mass galaxies. As a consequence, a large fraction of SNe is simulated in faint galaxies and are rejected as the OzDES selection function is applied. We note that small discrepancies are observed in the distribution of $g - r$ observed colours in the shallow fields, with a fraction of the red galaxies (mostly passive environments, primarily populated by SNe Ia) missing from simulations. This will be further investigated by implementing deeper and higher quality galaxy catalogues in the simulations.

From the Baseline simulation, we can predict the expected core-collapse SN contamination in the DES SN Ia sample. Table 3 summarizes how this contamination depends on the different SALT2 and light-curve cuts that can be applied. For the loose SALT2 cuts, we predict the fraction of non-Ia SNe to be around 22.5 per cent (2.6 per cent arising from peculiar SNe Ia, 5.7 per cent from SNe Ibc, and 14.2 per cent from SNe II), and for the Betoule et al. (2014) SALT2 cuts, the fraction decreases to 8.2 per cent (2.0 per cent from peculiar SNe Ia, 1.7 per cent from SNe Ibc, and 4.5 per cent from SNe II). We highlight that the SALT2 c and fit probability cuts remove the largest fraction of contamination.

SNe II are the largest source of contamination as they are the most common type of core-collapse SN, and the brightest SNe II are faster declining and therefore photometrically more similar to SNe Ia than the generally fainter plateauing SNe II. However, examining the Hubble residual distributions in Fig. 9 in detail we note that even

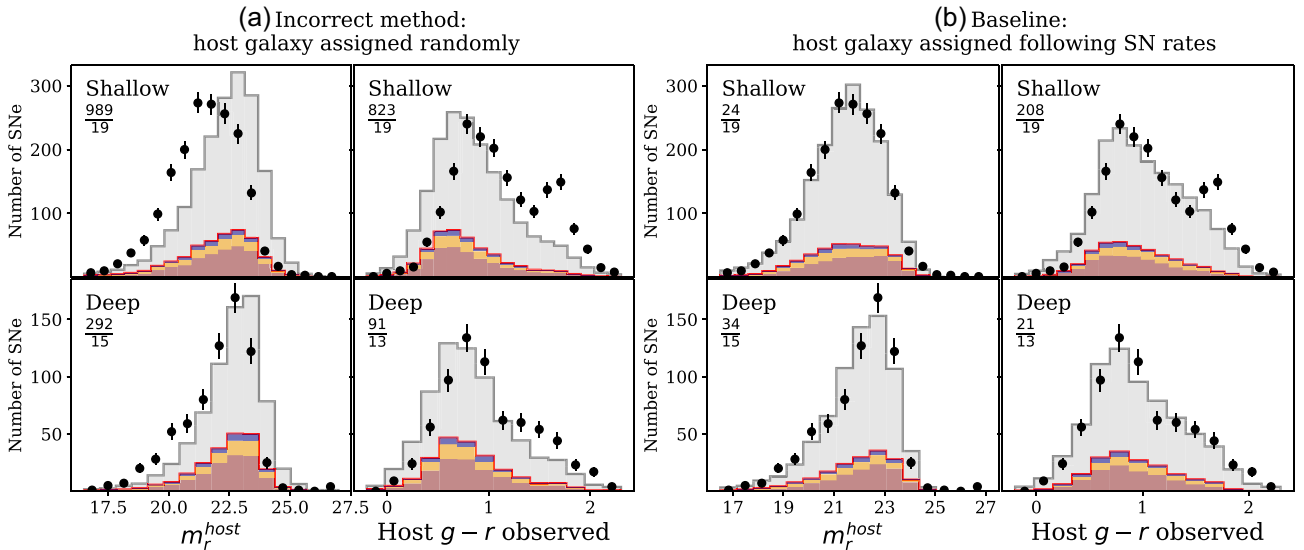


Figure 10. Same as Fig. 8, but for host galaxy m_r^{host} (left-hand panels) and host galaxy observed $g - r$ colours (right-hand panels). Panel (a) is for an incorrect implementation where host galaxies are assigned randomly to simulated SNe, while panel (b) uses our Baseline simulation.

Table 4. Summary of alternative simulations for core-collapse SNe.

Label	Template library	Luminosity functions	Dust model
Baseline	V19	Revised L11, Gaussian	NA ^a
Skewed LFs	V19	Revised L11, skewed Gaussian	NA
LFs + Offset	V19	Revised L11 + offset	NA
LFs z -evolving	V19	Revised L11 + z evolution	NA
Dust (H98)	Dereddened V19	Revised L11, Gaussian	Hatano, Branch & Deaton (1998)
Dust (R14)	Dereddened V19	Revised L11, Gaussian	Rodney et al. (2014)
Dust z -evolving	Dereddened V19	Revised L11, Gaussian	Hatano et al. (1998) + z evolution
J17	J17	Adjusted LFs from L11	NA
PLAsTiCC	PLAsTiCC	PLAsTiCC	NA

^aNA: not applicable – simulations with core-collapse SN templates that are *not* corrected for host dust extinction; additional extinction is not included.

though SNe Ibc are not the primary source of contamination, they have on average Hubble residuals closer to zero. In the next section, we discuss how the contamination fraction predicted in the Baseline simulation varies as different assumptions, modelling choices, and templates library are used.

6 TESTING ALTERNATIVE CORE-COLLAPSE SN SIMULATIONS

We next analyse how changing the assumptions and modelling choices discussed in Section 4.4 affects the results of this analysis and in particular the predicted fraction of core-collapse SN contamination in the DES sample. We use eight additional core-collapse SN simulations generated by adjusting the luminosity functions, the host galaxy dust extinction, and the SN colour dispersion, and using different libraries of core-collapse SN SED templates. The simulations are summarized in Table 4.

6.1 Luminosity functions

Luminosity functions, describing the distribution of absolute brightness of the SNe, are a critical element of uncertainty in our analysis. Due to the relative faintness of core-collapse SNe and thus the Malmquist biases inherent in SN surveys, luminosity functions are difficult to measure accurately and they depend on whether dust extinction corrections are applied (L11; Richardson et al. 2014). These corrections are generally uncertain, and it is difficult to disentangle the distribution of intrinsic brightness and the distribution of dust extinction. Currently, published measurements of core-collapse SN luminosity functions are based on local SNe (i.e. <100 Mpc). This low-redshift measurement adds further uncertainty as the properties of core-collapse SNe may evolve with redshift.

In our analysis, we model luminosity functions based on the volume-limited LOSS sample (Leaman et al. 2011; L11), taking into account the revised classification published by Shivvers et al. (2017). We explore different parametrizations, which we summarize in Table 5:

(i) We assume that the luminosity functions are described by a Gaussian distribution, corresponding to the Baseline simulation presented in Section 4.4;

(ii) We assume that the luminosity functions are described by a skewed Gaussian distribution (‘Skewed LFs’). Table 5 shows the parameters from skewed luminosity function fits to the revised LOSS sample: mean standard deviation and skewness. For all sub-types, we find a positive skewness, i.e. a larger tail on the fainter side of the

Table 5. Luminosity functions from L11 with revised classification from Shivvers et al. (2017).

SN type	Revised LFs from L11	
	Gaussian fit ^a	Skewed Gaussian fit ^b
II ^c	−15.97(1.31)	−17.51 (2.01, 3.18)
II _n	−17.90(0.95)	−19.13 (1.53, 6.83)
II _b	−16.69(1.38)	−18.30 (2.03, 7.40)
I _c	−16.75(0.97)	−17.51 (1.24, 1.22)
I _b	−16.07(1.34)	−17.71 (2.11, 7.15)
I _c /I _c -pec/I _c -BL	−16.79(0.95)	−17.74 (1.35, 2.06)

^aGaussian fit (mean with standard deviation in parenthesis) of the distributions of R -band absolute magnitudes for the bias-corrected LOSS sample. We use the Shivvers et al. (2017) classifications. Host extinction corrections are not applied.

^bSkewed Gaussian fit (mean with standard deviation and skewness in parenthesis) of the distributions of R -band absolute magnitudes for the bias-corrected LOSS sample. We use the Shivvers et al. (2017) classifications. Host extinction corrections are not applied.

^cFollowing the classification scheme introduced by Anderson et al. (2014) and applied by Shivvers et al. (2017), faster declining SNe II (often referred as SNe IIL) and slower SNe II (often referred as SNe IIP) are combined into a single SN II class.

luminosity distribution, compatible with the interpretation of dust extinction as the origin.

(iii) We apply a redshift-independent offset to the mean of each Gaussian luminosity function measured from the LOSS SN sample (‘LFs + Offset’). The uncertainty on the mean for the LOSS luminosity functions is typically 0.2–0.4 mag, and therefore adjustments within this range are consistent with the baseline values. However, Jones et al. (2017, hereafter J17) claim that the original LOSS luminosity functions need to be shifted by approximately -1 mag in order to match core-collapse SN contamination in the PanSTARRS SN sample. Here, we test the choice of an intermediate magnitude shift of -0.5 mag.

(iv) We introduce a redshift-dependent drift to the mean of the Gaussian luminosity functions (‘LF z -evolving’). This magnitude shift is $\Delta m = -0.5z$ mag and corresponds to a magnitude offset of -0.5 mag at $z = 1$.

In addition to the four alternative luminosity functions, we include luminosity functions implemented by J17 and in the PLAsTiCC simulations (these simulations are discussed in Section 6.3), with a total of six luminosity functions tested in this work. These luminosity functions are presented in Fig. 11 as distributions of Bessell R -band peak absolute magnitudes (for consistency with the luminosity functions presented by L11). The distributions are estimated as

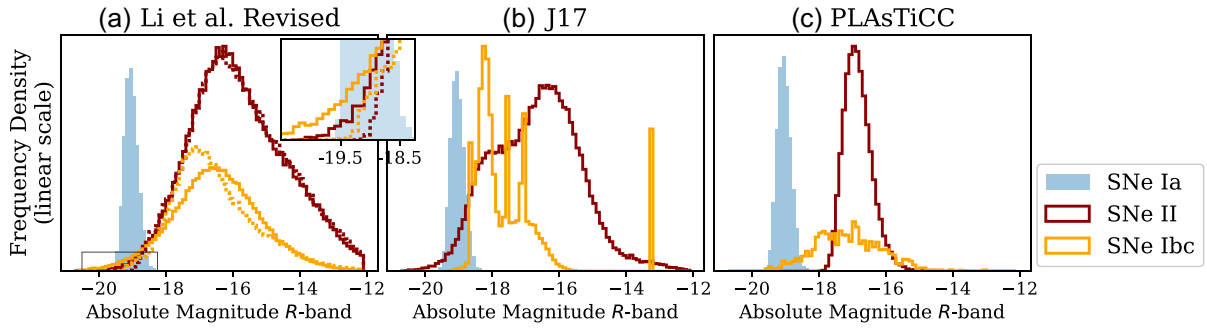


Figure 11. Distributions of simulated R -band absolute magnitudes at peak for various types of SNe. This series of panels summarizes the different core-collapse luminosity functions tested in this work. For visualization purposes, we also show the luminosity distribution of SNe Ia. The relative normalization between SNe Ia and core-collapse SNe is arbitrary, while the relative rate between stripped-envelope SNe (SNe Ibc) and hydrogen-rich SNe (SNe II) is preserved (roughly 0.435; see Shivvers et al. 2017). In panel (a), we use the luminosity functions presented by L11 and revised by V19. We present luminosity distributions derived using both the Gaussian parametrization (Baseline, solid line) and the skewed Gaussian parametrization (Skewed LFs, dotted lines). The analytical forms of the revised L11 luminosity functions are summarized in Table 5. The inset in the plot highlights differences in the brightest tail between the two parametrizations. In panel (b), we show luminosity distribution from the J17 core-collapse simulations; in panel (c), we show luminosity distributions estimated from simulations generated using the PLAsTiCC models (see Section 6.3).

follows. We consider the same input luminosity functions and templates designed for the DES core-collapse SN simulations tested in this work, and estimate the R -band peak absolute magnitudes from a set of 10 000 SN light curves and examine the distributions. These represent the effective underlying luminosity distributions used in each core-collapse SN simulation and allow a direct comparison between different luminosity functions. The distributions presented in the first panel of Fig. 11 match the analytical forms presented in Table 5.

6.2 Host galaxy extinction

The star-forming hosts of core-collapse SNe will typically contain high abundances of gas and dust and thus dust extinction within the host galaxy will be astrophysically important in our simulations. Two sets of V19 templates are available: one not corrected for host dust extinction (i.e. implicitly containing some extinction as observed in the SNe) and one corrected for dust extinction (see appendix A of V19, for more details). This allows two implementations of host galaxy extinction and two methods of matching simulated core-collapse SNe to luminosity functions. In the first approach, core-collapse SN events are simulated with their original host reddening, and the simulated luminosity function is adjusted to match the revised L11 luminosity functions. In the second approach, simulated core-collapse light-curves are synthesized from the *unreddened* SED models and applying arbitrary extinction models (thus augmenting the diversity; see Fig. 12). The luminosity distribution of the simulated events is matched to the revised L11 luminosity functions only *after* the extinction is applied.

We test both approaches and investigate different implementations of host dust extinction:

(i) We assume that the host extinguished V19 templates are representative of the core-collapse SN population in terms of extinction properties at all redshifts. In other words, we apply no further host extinction. This is our Baseline approach.

(ii) We use the set of de-reddened V19 SEDs and apply the host extinction distribution predicted by Hatano et al. (1998) [‘Dust (H98)’]. The distribution of B -band extinction (A_B) presented by Hatano et al. (1998) is converted into A_V and fitted with the sum of an exponential distribution, $\exp(-A_V/\tau)$, and a normal distribution

$\mathcal{N}(\mu, \sigma)$; we find $\tau = 0.05$, $\sigma = 0.5$, and $\mu = 0.45$. Fig. 13 shows the resulting distribution of simulated A_V . For this model, the median simulated extinction A_V is 0.35 mag.

(iii) We use the de-reddened V19 SEDs and the host extinction distribution used by Rodney et al. (2014) [‘Dust (R14)’]. This distribution is approximated with the same expression adopted for Hatano et al. (1998) but assuming $\tau = 1.7$, $\sigma = 0.6$, and $\mu = 0$. Fig. 13 shows the resulting distribution of simulated A_V . The choice of this distribution results in higher values of extinction, with median simulated A_V of 0.49 mag. This choice is motivated by the fact that other compilations of core-collapse SNe from untargeted surveys (i.e. surveys not primarily based on monitoring bright and typically dust-rich galaxies) seem to have larger mean extinction values (Prentice et al. 2016).

(iv) We use the de-reddened V19 SEDs and the host extinction distribution of Hatano et al. (1998), introducing a redshift dependence in the dust extinction. The dust content of a galaxy correlates with its SFR (Santini et al. 2014). Since the cosmic star formation increases by $\simeq 0.5$ dex between redshifts 0 and 1 (Madau & Dickinson 2014), we assume that the median simulated extinction A_V linearly increases by a factor of 3 to $z = 1$ (‘Dust z -evolving’) and apply a shift to the mean of the Gaussian component μ of $\Delta_\mu = 0.4z$ mag.

Figs 4(c) and 12(a) show the simulated $g - r$ colours at peak brightness for different approaches: the Baseline approach, and the approach where the distribution of dust from Hatano et al. (1998) is applied on the de-reddened templates [‘Dust (H98)’]. In the second case, the diversity of SN events simulated is significantly increased.

6.3 Comparing different libraries of templates

The most widely used library to date is that of the SNPhotCC (Kessler et al. 2010a, b), built from publicly available composite spectral time series⁷ adjusted to match multiband photometry for 41 well-observed, spectroscopically confirmed core-collapse SNe from various nearby photometric surveys. J17 augmented this library with additional templates of SNe IIb and 91bg-like SNe Ia.

In Fig. 11(b), we show the distribution of R -band absolute magnitudes derived from the J17 core-collapse SN simulations.

⁷https://c3.lbl.gov/nugent/nugent_templates.html

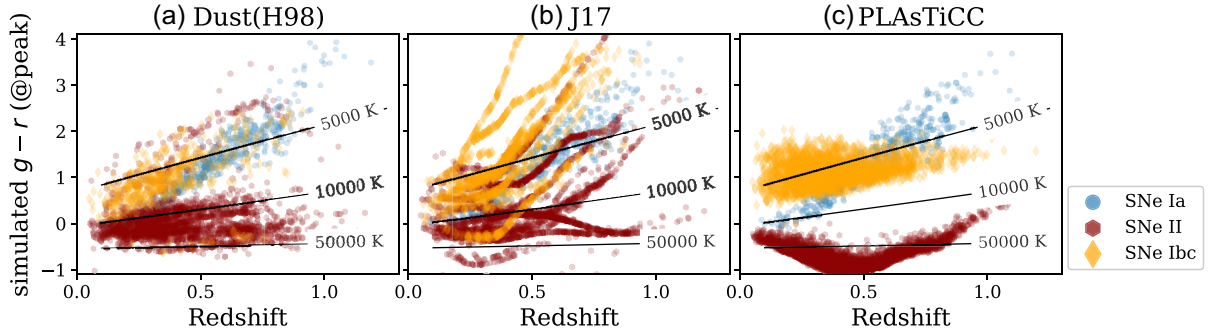


Figure 12. Simulated $g - r$ colour at peak brightness versus redshift for different SN types and templates. SNe Ia are generated as described in Section 4.2. Panel (a) is as panel (c) in Fig. 4, but using the V19 templates and a dust extinction distribution from Hatano et al. (1998). In panel (b), core-collapse SNe are simulated using the J17 set of templates and adjusted luminosity function. Panel (c): using PLAsTiCC models generated using MOSFIT for stripped-envelope SNe and non-negative matrix factorization for SNe II (see Section 6.3). We also show the $g - r$ colour measured from blackbody SEDs at temperatures of 5000, 10 000, and 50 000 K.

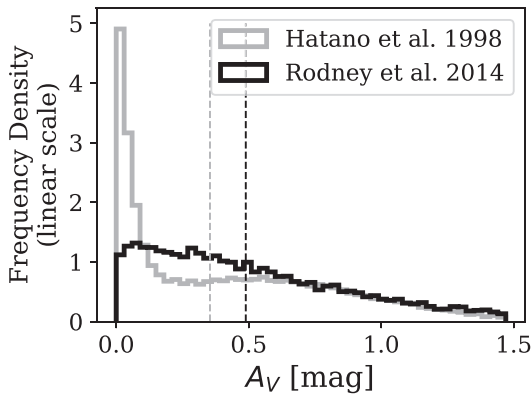


Figure 13. Simulated A_V extinction in Dust(H98) simulation (host dust extinction distribution from Hatano et al. 1998) and Dust(R14) simulation (host dust extinction distribution from Rodney et al. 2014); see Section 6.2 for more details. Dashed vertical lines show the median simulated A_V for each distribution.

J17 simulate SNe Ibc from a set of six SED templates without applying dispersion to the SED brightness, leading to the spikes in the luminosity function, and assume for SNe Ibc a luminosity function with the functional form $\mathcal{N}(-18.26, 0.15)$, explaining the brightest peak in the SN Ibc distribution. The bimodality for SNe II is due to SNe IIP and SNe IIL being modelled separately, following the rates and luminosity functions originally presented by L11. We note that the J17 templates lack a robust extension into the UV, and therefore at higher redshifts the simulation does not generate g -band observations (see Fig. 12b)

Kessler et al. (2019a) released a new library of core-collapse SN templates developed for PLAsTiCC, including two innovative approaches for simulating core-collapse SNe. For stripped-envelope SNe and SNe IIn, SED templates have been generated using the Modular Open-Source Fitter for Transients (MOSFIT; Guillochon et al. 2018) parametrization and following the theoretical models of Villar et al. (2017) for these two classes of transients. For SNe II, synthetic light curves were built applying dimensionality reduction techniques to a large sample of SN II multiband light curves. These techniques enable an order of magnitude increase in the number of SEDs generated (384 templates for SNe II, 836 for SNe IIn and stripped-envelope SNe). In Figs 11(c) and 12(c), we compare luminosity distributions and colour properties of core-collapse SNe generated using PLAsTiCC templates with other core-collapse SN

libraries. We note significant differences both in the distribution of simulated absolute magnitudes and in the colour evolution compared to simulations generated with V19 and J17 templates, especially for SNe II. In PLAsTiCC, the luminosity distribution of SNe II simulated light curves appears narrower than that expected from other measured luminosity functions, and drops to zero at -18 mag (although there are several fast-declining SNe II that have been observed to be brighter; Richardson et al. 2002; L11). Moreover, the simulated peak colour of these events is significantly bluer than that expected assuming a blackbody SED. This suggests that a revision of the SN II models implemented in PLAsTiCC may be required.

6.4 Analysis of Hubble residuals distributions

In Fig. 14, we present the simulated and observed Hubble residuals (equation 2) for each simulation (Table 4) and for the different SALT2 cuts (Section 2.4). Table 6 presents the predicted fraction of contamination from 91bg-like, SNe Iax, SNe Ibc, and SNe II, and the total contamination, for shallow and deep fields separately. Finally, Table 7 presents the χ^2_v of Hubble residual distributions. χ^2_v are estimated both for Hubble residuals < 0.5 (the ‘SN Ia-dominated’ region) and > 0.5 (the ‘core-collapse SN-dominated’ region).

Generally, the agreement is good. As noted for the Baseline simulation, the largest discrepancies are found at zero and negative Hubble residuals where the contamination is small (Fig. 14), and this drives the large value of χ^2_v (Table 7). When loose SALT2 cuts are applied, more significant discrepancies are found in the core-collapse SN simulations where the luminosity functions are artificially brightened (‘LFs z -evolving’ and ‘LFs + Offset’). These simulations overestimate the number of SNe with Hubble residuals > 0.5 by approximately 20–25 per cent, disfavouring such adjustments. Simulations where larger host extinctions are applied [‘Dust (R14)’ and ‘Dust z -evolving’] underestimate the number of SNe with Hubble residuals < 0.5 by 10 per cent.

When the cuts from Betoule et al. (2014) are applied, the simulations accurately predict the number of events with large Hubble residuals ($HR > 0.5$), with χ^2_v values between 0.7 to 1.2 (Table 6). The large discrepancies observed when applying only loose SALT2-based cuts in simulations (LFs + Offset and LFs z -evolving) appear to be partially resolved when tighter SALT2 cuts are applied. This suggests that understanding how SALT2-based cuts affect core-collapse contamination is an important aspect in this type of analysis.

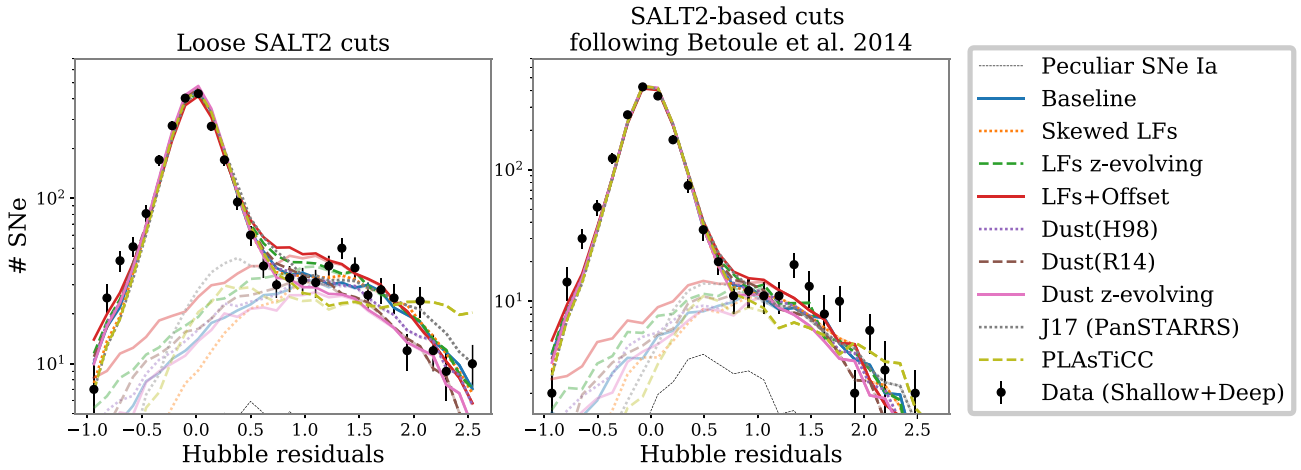


Figure 14. Distributions of observed and simulated Hubble residuals for the full range of simulations. Distributions are presented for the data (shallow and deep fields combined, black symbols) and for the nine simulations summarized in Table 4 (see Section 6): Both SNe Ia and core-collapse SNe are combined in the darker lines, and only simulated core-collapse SNe are shown in the partially transparent lines. *Left:* Sample selected applying loose SALT2-based cuts ($x_1 \in [-4.9, 4.9]$ and SALT2 $c \in [-0.49, 0.49]$). The fraction of core-collapse SNe for each simulation is reported in Table 6 and is approximately a fourth of the sample. *Right:* SALT2-based cuts from Betoule et al. (2014) are applied. The fraction of core-collapse SNe in the simulations is reported in Table 6.

Table 6. True fraction of contamination (averaged over 25 realizations).

	Non-Ia fraction (per cent)	Loose SALT2 cuts		Non-Ia fraction in shallow and deep (per cent)	Non-Ia fraction (per cent)	SALT2 cuts following Betoule et al. (2014)	
		Fraction of 91bg, Iax, Ibc, II (per cent)				Fraction of Iax, Ibc, II ^a (per cent)	Non-Ia fraction in shallow and deep (per cent)
Baseline	22.5	0.1, 2.5, 5.7, 14.2		21.6, 24.5	8.2	2.0, 1.7, 4.5	7.9, 8.8
Skewed LFs	20.4	0.1, 2.6, 4.4, 13.2		19.5, 22.5	7.5	2.0, 1.4, 4.1	7.2, 8.2
LFs z-evolving	27.5	0.1, 2.4, 7.1, 17.8		26.4, 30.0	9.9	2.0, 2.3, 5.7	9.5, 11.0
LFs + Offset	31.7	0.1, 2.2, 8.6, 20.7		30.8, 33.6	11.7	1.9, 3.0, 6.7	11.4, 12.6
Dust(H98)	22.0	0.1, 2.6, 6.1, 13.2		21.1, 24.1	8.5	2.0, 2.2, 4.2	8.1, 9.4
Dust(R14)	21.6	0.1, 2.6, 5.6, 13.3		20.8, 23.6	8.4	2.0, 1.9, 4.5	7.9, 9.6
Dust z-evolving	18.6	0.1, 2.7, 4.9, 10.9		17.8, 20.4	7.2	2.0, 1.6, 3.6	6.8, 8.0
J17 (PanSTARRS)	28.5	0.1, 2.4, 11.5, 14.5		27.3, 31.2	8.7	2.0, 3.5, 3.1	8.1, 10.1
PLAsTiCC	24.6	0.1, 2.5, 7.3, 14.3		23.1, 27.9	7.0	2.0, 2.1, 2.8	6.5, 8.1

^aAfter SALT2-based cuts following Betoule et al. (2014) are applied, the predicted fraction of 91bg-like SNe Ia is less than 0.1 per cent.

Table 7. χ^2_v between observed and simulated events for different Hubble residual ranges.

	Loose SALT2 cuts		Betoule et al. (2014) SALT2 cuts	
	HR < 0.5	HR > 0.5	HR < 0.5	HR > 0.5
<i>SNe Ia only</i>	5.3	60.3	4.3	22.6
<i>Peculiar Ia only</i> ^a	5.0	29.3	4.3	7.5
Baseline	4.2	1.9	4.1	1.0
Skewed LFs	4.9	1.5	4.2	1.0
LFs z-evolving	3.9	1.8	4.0	1.2
LFs + Offset	4.1	1.8	4.1	1.3
Dust(H98)	4.0	1.7	4.1	1.2
Dust(R14)	4.0	2.4	4.0	1.4
Dust z-evolving	4.2	2.0	4.1	1.3
J17 (PanSTARRS)	6.6	3.1	4.8	1.4
PLAsTiCC	5.5	10.3	4.5	2.0

^aSimulation generated including only SNe Ia and peculiar SNe Ia, SNe Iax, and 91bg-like SNe Ia.

The ‘Skewed LFs’ simulation predicts one of the lowest values of core-collapse SN contamination. As shown in Fig. 11, a skewed Gaussian parametrization of the luminosity functions produces less bright events compared to a Gaussian parametrization of the luminosity functions. This shows that simulation of core-collapse SNe is sensitive to how the brighter tails of the luminosity functions are modelled. Finally, we note that the PLAsTiCC simulation shows

poor agreement with the data, both before and after SALT2-based cuts. We suggest that the main cause of this disagreement is an incomplete modelling of SNe II (see Section 6.3).

Overall, the range of contamination predicted by our simulations is small, with a minimum of 7.2 per cent of contamination predicted from the ‘Dust z-evolving LFs’ simulation (excluding PLAsTiCC simulation) to a maximum of 11.7 per cent contamination in the ‘LFs + Offset’ simulation. The average contamination among the different tested scenarios is 8.8 per cent, and the r.m.s is 1.1 per cent. We note that this is the contamination expected in the photometric DES SN sample prior to the application of any photometric classification algorithm. After photometric classification, the typical contamination expected is likely to decrease substantially (Möller & de Boissière 2020, Vincenzi et al., in preparation).

7 SUMMARY AND FUTURE WORK

We have presented a set of simulations designed to reproduce the DES photometric SN sample. The DES photometric SN sample includes more than 2500 SNe with high-quality multiband photometry and spectroscopic redshifts from the identified SN host galaxies. It is the largest sample of photometrically identified SNe Ia to date and in this work we described how the sample has been collected and what are the relevant cuts we applied to filter non-SN transients.

Our focus in this paper has been to model and reproduce with simulations the population of contaminants observed in the DES photometric sample, where we define as contaminants transients that are photometrically similar to SNe Ia but are not standardizable candles, i.e. peculiar SNe Ia and core-collapse SNe. The simulations presented in this work are a significant improvement compared to previously published mock catalogues of photometric SN samples. The principal advances are as follows:

- (i) We use core-collapse SNe that are synthesized from high-quality templates. We explore different methods for implementing host galaxy dust extinction and different luminosity functions, and we demonstrate that the diversity and quality of the simulated core-collapse SN light curves are significantly improved;
- (ii) We use a host-galaxy spectroscopic redshift efficiency that is modelled as a three-dimensional function of host galaxy brightness, observed colours, and year of SN discovery. This efficiency function has been measured by analysing the sample of galaxies that hosted DES SN candidates and comparing those for which a spectroscopic redshift was obtained and those for which it was not;
- (iii) We simulate SN host galaxies using published SN rates and their dependence on host galaxy properties. This ensures that each sub-type of transient is associated with a physically meaningful population of galaxies. This, combined with our measured efficiency function, enables us to accurately model selection effects for every type of transient, every type of galaxy, and every redshift range.

The ultimate test to verify whether our simulations are realistic and physically accurate is to compare the simulated samples with the real data. We find excellent agreement between our simulations and the DES SN sample, when both loose and cosmology-like SALT2-based cuts are applied. From our baseline simulation, we predict the fraction of core-collapse SN contamination in the DES SN sample to be 8.2 per cent after applying SALT2-based cuts similar to those in the cosmological analysis from Betoule et al. (2014).

We additionally explore alternative template libraries, luminosity functions, and host galaxy dust extinction models. We consider nine core-collapse SN scenarios, designed to span a wide range of modelling choices. We analyse this set of simulations and find that the majority reproduce observed contamination well (with measured χ^2_ν between 1. and 1.4 for large Hubble residuals) and that the predicted core-collapse contamination varies between 7.2 and 11.7 per cent, with an average of 8.8 and an r.m.s. of 1.1. This suggests that, although our knowledge of the global properties of core-collapse SNe remains incomplete, core-collapse SN contamination in the DES photometric SN sample can be well constrained.

While the agreement between data and simulations is already good, some discrepancies remain and we anticipate improvements from future analyses. Different ways of increasing the depth of the galaxy library implemented in our simulations will be explored, either using observations (i.e. deep coadds published by Wiseman et al. 2020) or simulations (SkyPy Collaboration 2020). Additionally, the modelling of SN Ia intrinsic properties and contribution of the host galaxy to the observational noise will be studied.

This work lays the foundation for several analyses central to the cosmological analysis of the DES photometric SN survey. The cosmological constraints obtained will depend more on our ability to validate the true contamination rather than obtaining the smallest prediction for that contamination. In future papers, we will use the simulations presented here to train and test the photometric classifiers that will be implemented in the cosmological analysis of the DES SN sample. We will also measure systematic uncertainties and potential biases in cosmological measurements due to core-

collapse SN contamination. Finally, the methods and techniques used in this work constitute a powerful tool to predict core-collapse SN contamination in future cosmological SN Ia samples and can be applied to simulate SNe in time-domain surveys like the 10-yr LSST (Ivezić et al. 2019) and surveys with the *Nancy Grace Roman Space Telescope* (Hounsell et al. 2018).

ACKNOWLEDGEMENTS

This work was supported by the Science and Technology Facilities Council (grant number ST/P006760/1) through the DISCnet Centre for Doctoral Training. MS acknowledges support from EU/FP7-ERC grant 615929, and PW acknowledges support from STFC grant ST/R000506/1. LG was funded by the European Union's Horizon 2020 research and innovation programme under the Marie Skłodowska-Curie grant agreement number 839090. This work has been partially supported by the Spanish grant PGC2018-095317-B-C21 within the European Funds for Regional Development (FEDER). RH and MS were supported by DOE grant DE-FOA-0001781 and NASA grant NNH15ZDA001N-WFIRST. The material is based on work supported by NASA under award number 80GSFC17M0002.

This paper has gone through internal review by the DES collaboration. Funding for the DES Projects has been provided by the U.S. Department of Energy, the U.S. National Science Foundation, the Ministry of Science and Education of Spain, the Science and Technology Facilities Council of the United Kingdom, the Higher Education Funding Council for England, the National Center for Supercomputing Applications at the University of Illinois at Urbana-Champaign, the Kavli Institute of Cosmological Physics at the University of Chicago, the Center for Cosmology and Astro-Particle Physics at the Ohio State University, the Mitchell Institute for Fundamental Physics and Astronomy at Texas A&M University, Financiadora de Estudos e Projetos, Fundação Carlos Chagas Filho de Amparo à Pesquisa do Estado do Rio de Janeiro, Conselho Nacional de Desenvolvimento Científico e Tecnológico and the Ministério da Ciência, Tecnologia e Inovação, the Deutsche Forschungsgemeinschaft, and the Collaborating Institutions in the Dark Energy Survey.

The Collaborating Institutions are Argonne National Laboratory, the University of California at Santa Cruz, the University of Cambridge, Centro de Investigaciones Energéticas, Medioambientales y Tecnológicas-Madrid, the University of Chicago, University College London, the DES-Brazil Consortium, the University of Edinburgh, the Eidgenössische Technische Hochschule (ETH) Zürich, Fermi National Accelerator Laboratory, the University of Illinois at Urbana-Champaign, the Institut de Ciències de l'Espai (IEEC/CSIC), the Institut de Física d'Altes Energies, Lawrence Berkeley National Laboratory, the Ludwig-Maximilians Universität München and the associated Excellence Cluster Universe, the University of Michigan, NFS's NOIRLab, the University of Nottingham, The Ohio State University, the University of Pennsylvania, the University of Portsmouth, SLAC National Accelerator Laboratory, Stanford University, the University of Sussex, Texas A&M University, and the OzDES Membership Consortium.

Based in part on observations at Cerro Tololo Inter-American Observatory at NSF's NOIRLab (NOIRLab Prop. ID 2012B-0001; PI: J. Frieman), which is managed by the Association of Universities for Research in Astronomy (AURA) under a cooperative agreement with the National Science Foundation.

The DES data management system is supported by the National Science Foundation under grant numbers AST-1138766 and AST-1536171. The DES participants from Spanish institutions

are partially supported by MICINN under grants ESP2017-89838, PGC2018-094773, PGC2018-102021, SEV-2016-0588, SEV-2016-0597, and MDM-2015-0509, some of which include ERDF funds from the European Union. IFAE is partially funded by the CERCA program of the Generalitat de Catalunya. Research leading to these results has received funding from the European Research Council under the European Union's Seventh Framework Program (FP7/2007-2013) including ERC grant agreements 240672, 291329, and 306478. We acknowledge support from the Brazilian Instituto Nacional de Ciência e Tecnologia (INCT) do e-Universo (CNPq grant 465376/2014-2).

This manuscript has been authored by Fermi Research Alliance, LLC under Contract No. DE-AC02-07CH11359 with the U.S. Department of Energy, Office of Science, Office of High Energy Physics.

Finally, this work was based in part on data acquired at the AAT, under program A/2013B/012. We acknowledge the traditional owners of the land on which the AAT stands, the Gamilaraay people, and pay our respects to elders past and present.

DATA AVAILABILITY

Input and configuration files needed to reproduce the simulations using the software SNANA are made available at https://github.com/maria-vincenzi/DES_CC_simulations. Data relative to the DES photometric sample used in Figs 8, 9, 10, and 14 are also made available (counts per each bin for all distributions presented in the figures).

REFERENCES

- Abbott T. M. C. et al., 2019, *Phys. Rev. Lett.*, 122, 171301
- Ahumada R. et al., 2020, *ApJS*, 249, 3
- Anderson J. P. et al., 2014, *ApJ*, 786, 67
- Astier P. et al., 2006, *A&A*, 447, 31
- Astier P. et al., 2013, *A&A*, 557, A55
- Baker A. J., Blyth S., Holwerda B., 2019, American Astronomical Society Meeting Abstracts #233, p. 333.01
- Baldry I. K. et al., 2018, *MNRAS*, 474, 3875
- Bertin E., Arnouts S., 1996, *A&AS*, 117, 393
- Betoule M. et al., 2014, *A&A*, 568, A22
- Boone K., 2019, *ApJ*, 158, 257
- Bradshaw E. J. et al., 2013, *MNRAS*, 433, 194
- Brout D., Scolnic D., 2020, *ApJ*, 909, 26
- Brout D. et al., 2019a, *ApJ*, 874, 106
- Brout D. et al., 2019b, *ApJ*, 874, 150
- Campbell H. et al., 2013, *ApJ*, 763, 88
- Cardelli J. A., Clayton G. C., Mathis J. S., 1989, *ApJ*, 345, 245
- Childress M. J. et al., 2017, *MNRAS*, 472, 273
- Chornock R., Filippenko A. V., Branch D., Foley R. J., Jha S., Li W., 2006, *PASP*, 118, 722
- Colless M. et al., 2003, preprint ([astro-ph/0306581](https://arxiv.org/abs/astro-ph/0306581))
- Dark Energy Survey, 2019a, *Phys. Rev. Lett.*, 122, 171301
- Dark Energy Survey, 2019b, *ApJ*, 872, L30
- Davies L. J. M. et al., 2018, *MNRAS*, 480, 768
- Dilday B. et al., 2008, *ApJ*, 682, 262
- Filippenko A. V. et al., 1992, *AJ*, 104, 1543
- Flaugher B. et al., 2015, *AJ*, 150, 150
- Foley R. J. et al., 2013, *ApJ*, 767, 57
- Frohmaier C., Sullivan M., Nugent P. E., Goldstein D. A., DeRose J., 2017, *ApJS*, 230, 4
- Frohmaier C. et al., 2019, *MNRAS*, 486, 2308
- Frohmaier C. et al., 2021, *MNRAS*, 500, 5142
- Geha M. et al., 2017, *ApJ*, 847, 4
- Goldstein D. A. et al., 2015, *AJ*, 150, 82
- Graur O., Bianco F. B., Huang S., Modjaz M., Shivvers I., Filippenko A. V., Li W., Eldridge J. J., 2017, *ApJ*, 837, 120
- Graur O., Bianco F. B., Modjaz M., 2015, *MNRAS*, 450, 905
- Guillochon J., Nicholl M., Villar V. A., Mockler B., Narayan G., Mandel K. S., Berger E., Williams P. K. G., 2018, *ApJS*, 236, 6
- Gupta R. R. et al., 2016, *AJ*, 152, 154
- Guy J. et al., 2007, *A&A*, 466, 11
- Guy J. et al., 2010a, *A&A*, 523, A7
- Hatano K., Branch D., Deaton J., 1998, *ApJ*, 502, 177
- Herenz E. C. et al., 2017, *A&A*, 606, A12
- Hinton S., Brout D., 2020, *J. Open Source Softw.*, 5, 2122
- Hložek R. et al., 2020, preprint ([arXiv:2012.12392](https://arxiv.org/abs/2012.12392))
- Holtzman J. A. et al., 2008, *AJ*, 136, 2306
- Hounsell R. et al., 2018, *ApJ*, 867, 23
- Howell D. A., 2001, *ApJ*, 554, L193
- Ivezić Ž. et al., 2019, *ApJ*, 873, 111
- Jha S. W., 2017, Handbook of Supernovae. Springer Int. Publ. AG, Berlin, p. 375
- Johansson J. et al., 2013, *MNRAS*, 435, 1680
- Jones D. O. et al., 2017, *ApJ*, 843, 6 (J17)
- Jones D. O. et al., 2018, *ApJ*, 857, 51
- Jones D. O. et al., 2019, *ApJ*, 881, 19
- Kelly P. L., Kirshner R. P., 2012, *ApJ*, 759, 107
- Kelly P. L., Kirshner R. P., Pahre M., 2008, *ApJ*, 687, 1201
- Kessler R., Conley A., Jha S., Kuhlmann S., 2010a, preprint ([arXiv:1001.5210](https://arxiv.org/abs/1001.5210))
- Kessler R. et al., 2009, *PASP*, 121, 1028
- Kessler R. et al., 2010b, *PASP*, 122, 1415
- Kessler R. et al., 2013, *ApJ*, 764, 48
- Kessler R. et al., 2015, *AJ*, 150, 172
- Kessler R. et al., 2019a, *PASP*, 131, 094501
- Kessler R. et al., 2019b, *MNRAS*, 485, 1171 (K19)
- Lampeitl H. et al., 2010, *ApJ*, 722, 566
- Lasker J. et al., 2019, *MNRAS*, 485, 5329
- Law N. M. et al., 2009, *PASP*, 121, 1395
- Leaman J., Li W., Chornock R., Filippenko A. V., 2011, *MNRAS*, 412, 1419
- Le Fèvre O. et al., 2013, *A&A*, 559, A14
- Lidman C. et al., 2020, *MNRAS*, 496, 19
- Li W. et al., 2003, *PASP*, 115, 453
- Li W. et al., 2011, *MNRAS*, 412, 1441 (L11)
- Lochner M., McEwen J. D., Peiris H. V., Lahav O., Winter M. K., 2016, *ApJS*, 225, 31
- Macaulay E. et al., 2019, *MNRAS*, 486, 2184
- Madau P., Dickinson M., 2014, *ARA&A*, 52, 415
- Mannucci F., Della Valle M., Panagia N., Cappellaro E., Cresci G., Maiolino R., Petrosian A., Turatto M., 2005, *A&A*, 433, 807
- Mao M. Y., Sharp R., Saikia D. J., Norris R. P., Johnston-Hollitt M., Middelberg E., Lovell J. E. J., 2010, *MNRAS*, 406, 2578
- Möller A., de Boissière T., 2020, *MNRAS*, 491, 4277
- Muzzin A. et al., 2012, *ApJ*, 746, 188
- Nanayakkara T. et al., 2016, *ApJ*, 828, 21
- Newman J. A. et al., 2013, *ApJS*, 208, 5
- Paterno M., 2004, Calculating efficiencies and their uncertainties
- Perley D. A. et al., 2020, *ApJ*, 904, 35
- Perrett K. et al., 2012, *ApJ*, 144, 59
- Phillips M. M. et al., 2007, *PASP*, 119, 360
- Planck Collaboration VI, 2020, *A&A*, 641, A6
- Popovic B., Brout D., Kessler R., Scolnic D., Lu L., 2021, *ApJ*, 913, id. 49
- Popovic B., Scolnic D., Kessler R., 2020, *ApJ*, 890, 172
- Prentice S. J. et al., 2016, *MNRAS*, 458, 2973
- Richardson D., Branch D., Casebeer D., Millard J., Thomas R. C., Baron E., 2002, *AJ*, 123, 745
- Richardson D., Jenkins R. L., III, Wright J., Maddox L., 2014, *AJ*, 147, 118
- Rigault M. et al., 2018, *A&A*, 644, A176
- Rodney S. A. et al., 2014, *AJ*, 148, 13
- Rykoff E. S. et al., 2016, *ApJS*, 224, 1

- Sahu D. K. et al., 2008, *ApJ*, 680, 580
- Sako M. et al., 2011, *ApJ*, 738, 162
- Santini P. et al., 2014, *A&A*, 562, A30
- Scodreggio M. et al., 2018, *A&A*, 609, A84
- Scolnic D., Kessler R., 2016, *ApJ*, 822, L35
- Scolnic D. et al., 2019, *Astro2020: Decadal Survey*, 2020, 270
- Scolnic D. M. et al., 2018, *ApJ*, 859, 101
- Sérsic J. L., 1963, *Bol. Asociacion Argentina Astron. La Plata Argentina*, 6, 41
- Shivvers I. et al., 2017, *PASP*, 129, 054201
- Silverman J. M. et al., 2012, *MNRAS*, 425, 1789
- SkyPy Collaboration, 2020, *SkyPy*
- Smith M. et al., 2012, *ApJ*, 755, 61
- Smith M. et al., 2020a, *AJ*, 160, 267
- Smith M. et al., 2020b, *MNRAS*, 494, 4426
- Stahl B. E. et al., 2019, *MNRAS*, 490, 3882
- Strolger L.-G. et al., 2015, *ApJ*, 813, 93
- Sullivan M. et al., 2006, *ApJ*, 648, 868
- Sullivan M. et al., 2010, *MNRAS*, 406, 782
- Takaro T. et al., 2020, *MNRAS*, 493, 986
- Tasca L. A. M. et al., 2017, *A&A*, 600, A110
- The PLAsTiCC Team et al., 2018, preprint ([arXiv:1810.00001](https://arxiv.org/abs/1810.00001))
- Tripp R., 1998, *A&A*, 331, 815
- Villar V. A., Berger E., Metzger B. D., Guillochon J., 2017, *ApJ*, 849, 70
- Vincenzi M., Sullivan M., Firth R. E., Gutiérrez C. P., Frohmaier C., Smith M., Angus C., Nichol R. C., 2019, *MNRAS*, 489, 5802 (V19)
- Weiner B. J. et al., 2005, *ApJ*, 620, 595
- Wiseman P. et al., 2020, *MNRAS*, 495, 4040
- Wiseman P. et al., 2021, preprint ([arXiv:2105.11954](https://arxiv.org/abs/2105.11954))
- Yuan F. et al., 2015, *MNRAS*, 452, 3047
- ¹*Institute of Cosmology and Gravitation, University of Portsmouth, Portsmouth PO1 3FX, UK*
- ²*School of Physics and Astronomy, University of Southampton, Southampton SO17 1BJ, UK*
- ³*Department of Astrophysics, American Museum of Natural History, New York, NY 10024, USA*
- ⁴*Center for Astrophysics, Harvard & Smithsonian, 60 Garden Street, Cambridge, MA 02138, USA*
- ⁵*School of Mathematics and Physics, University of Queensland, Brisbane, QLD 4072, Australia*
- ⁶*PITT PACC, Department of Physics and Astronomy, University of Pittsburgh, Pittsburgh, PA 15260, USA*
- ⁷*University of Maryland, Baltimore County, 1000 Hilltop Circle, Baltimore, MD 21250, USA*
- ⁸*NASA Goddard Space Flight Center, 8800 Greenbelt Road, Greenbelt, MD 20771, USA*
- ⁹*Department of Physics and Astronomy, University of Pennsylvania, Philadelphia, PA 19104, USA*
- ¹⁰*Department of Astronomy and Astrophysics, University of Chicago, Chicago, IL 60637, USA*
- ¹¹*Kavli Institute for Cosmological Physics, University of Chicago, Chicago, IL 60637, USA*
- ¹²*Argonne National Laboratory, 9700 South Cass Avenue, Lemont, IL 60439, USA*
- ¹³*Centre for Gravitational Astrophysics, College of Science, Australian National University, Canberra, ACT 2601, Australia*
- ¹⁴*The Research School of Astronomy and Astrophysics, Australian National University, Canberra, ACT 2601, Australia*
- ¹⁵*Laboratoire de Physique de Clermont, Université Clermont Auvergne, CNRS/IN2P3, LPC, F-63000 Clermont-Ferrand, France*
- ¹⁶*Department of Physics, Duke University Durham, Durham, NC 27708, USA*
- ¹⁷*Centro de Investigaciones Energéticas, Medioambientales y Tecnológicas (CIEMAT), Madrid, 28040, Spain*
- ¹⁸*Sydney Institute for Astronomy, School of Physics, A28, The University of Sydney, Sydney, NSW 2006, Australia*
- ¹⁹*Departamento de Física Matemática, Instituto de Física, Universidade de São Paulo, CP 66318, São Paulo, SP 05314-970, Brazil*
- ²⁰*Laboratório Interinstitucional de e-Astronomia – LIneA, Rua Gal. José Cristino 77, Rio de Janeiro, RJ 20921-400, Brazil*
- ²¹*Fermi National Accelerator Laboratory, PO Box 500, Batavia, IL 60510, USA*
- ²²*Instituto de Física Teórica UAM/CSIC, Universidad Autónoma de Madrid, E-28049 Madrid, Spain*
- ²³*CNRS, UMR 7095, Institut d’Astrophysique de Paris, F-75014 Paris, France*
- ²⁴*Institut d’Astrophysique de Paris, Sorbonne Universités, UPMC Paris 06, UMR 7095, F-75014 Paris, France*
- ²⁵*Department of Physics & Astronomy, University College London, Gower Street, London WC1E 6BT, UK*
- ²⁶*Kavli Institute for Particle Astrophysics & Cosmology, Stanford University, PO Box 2450, Stanford, CA 94305, USA*
- ²⁷*SLAC National Accelerator Laboratory, Menlo Park, CA 94025, USA*
- ²⁸*Instituto de Astrofísica de Canarias, E-38205 La Laguna, Tenerife, Spain*
- ²⁹*Departamento Astrofísica, Universidad de La Laguna, E-38206 La Laguna, Tenerife, Spain*
- ³⁰*Department of Astronomy, University of Illinois at Urbana–Champaign, 1002 W. Green Street, Urbana, IL 61801, USA*
- ³¹*National Center for Supercomputing Applications, 1205 West Clark Street, Urbana, IL 61801, USA*
- ³²*Institut de Física d’Altes Energies (IFAE), The Barcelona Institute of Science and Technology, Campus UAB, E-08193 Bellaterra (Barcelona), Spain*
- ³³*Institut d’Estudis Espacials de Catalunya (IEEC), E-08034 Barcelona, Spain*
- ³⁴*Institute of Space Sciences (ICE, CSIC), Campus UAB, Carrer de Can Magrans, s/n, E-08193 Barcelona, Spain*
- ³⁵*Center for Cosmology and Astro-Particle Physics, The Ohio State University, Columbus, OH 43210, USA*
- ³⁶*INAF – Osservatorio Astronomico di Trieste, Via G. B. Tiepolo 11, I-34143 Trieste, Italy*
- ³⁷*Institute for Fundamental Physics of the Universe, Via Beirut 2, I-34014 Trieste, Italy*
- ³⁸*Observatório Nacional, Rua Gal. José Cristino 77, Rio de Janeiro, RJ 20921-400, Brazil*
- ³⁹*Department of Physics, University of Michigan, Ann Arbor, MI 48109, USA*
- ⁴⁰*Department of Physics, IIT Hyderabad, Kandi, Telangana 502285, India*
- ⁴¹*Santa Cruz Institute for Particle Physics, Santa Cruz, CA 95064, USA*
- ⁴²*Institute of Theoretical Astrophysics, University of Oslo, PO Box 1029, Blindern, NO-0315 Oslo, Norway*
- ⁴³*Department of Astronomy, University of Michigan, Ann Arbor, MI 48109, USA*
- ⁴⁴*Department of Physics, Stanford University, 382 Via Pueblo Mall, Stanford, CA 94305, USA*
- ⁴⁵*Department of Physics, The Ohio State University, Columbus, OH 43210, USA*
- ⁴⁶*Faculty of Physics, Ludwig-Maximilians-Universität, Scheinerstr 1, D-81679 Munich, Germany*
- ⁴⁷*Max Planck Institute for Extraterrestrial Physics, Giessenbachstrasse, D-85748 Garching, Germany*
- ⁴⁸*Universitäts-Sternwarte, Fakultät für Physik, Ludwig-Maximilians Universität München, Scheinerstr 1, D-81679 München, Germany*
- ⁴⁹*Center for Astrophysics | Harvard & Smithsonian, 60 Garden Street, Cambridge, MA 02138, USA*
- ⁵⁰*Australian Astronomical Optics, Macquarie University, North Ryde, NSW 2113, Australia*
- ⁵¹*Lowell Observatory, 1400 Mars Hill Road, Flagstaff, AZ 86001, USA*
- ⁵²*Department of Astronomy, The Ohio State University, Columbus, OH 43210, USA*
- ⁵³*Radcliffe Institute for Advanced Study, Harvard University, Cambridge, MA 02138, USA*
- ⁵⁴*Institució Catalana de Recerca i Estudis Avançats, E-08010 Barcelona, Spain*

⁵⁵*Physics Department, University of Wisconsin–Madison, 1150 University Avenue, Madison, WI 53706-1390, USA*

⁵⁶*Institute of Astronomy, University of Cambridge, Madingley Road, Cambridge CB3 0HA, UK*

⁵⁷*Department of Astrophysical Sciences, Princeton University, Peyton Hall, Princeton, NJ 08544, USA*

⁵⁸*Department of Physics and Astronomy, Pevensey Building, University of Sussex, Brighton BN1 9QH, UK*

⁵⁹*Computer Science and Mathematics Division, Oak Ridge National Laboratory, Oak Ridge, TN 37831, USA*

⁶⁰*Cerro Tololo Inter-American Observatory, NSF's National Optical-Infrared Astronomy Research Laboratory, Casilla 603, La Serena, 2760, Chile*

This paper has been typeset from a \TeX/L\TeX file prepared by the author.